

ABSTRACT

Title of Thesis: CHARACTERIZATION OF SUBCELLS IN
MULTIJUNCTION SOLAR CELLS USING
ELECTROLUMINESCENCE

Sai Meghasena Chavali, Master of Science,
2020

Thesis Directed By: Professor Mario Dagenais, ECE
Dr. Behrang Hamadani, National Institutes of
Standards and Technology (NIST)

Each subcell in a multijunction solar cell has different material properties that allow for absorption of a certain range of the solar spectrum. However, the power conversion efficiency and the various photovoltaic losses are different for each subcell and are not easily characterized because the subcells are series-connected within the cell stack. In this thesis, it is demonstrated that detailed characterization of each subcell can be accomplished by measuring the absolute electroluminescence response of the solar cell using a hyperspectral imaging system. The instrumentation used and the methodology to calculate the efficiency and loss parameters are detailed in this work and the physical characteristics of three types of multijunction devices are compared with each other.

CHARACTERIZATION OF SUBCELLS IN MULTIJUNCTION SOLAR CELLS
USING ELECTROLUMINESCENCE

by

Sai Meghasena Chavali

Thesis submitted to the Faculty of the Graduate School of the
University of Maryland, College Park, in partial fulfillment
of the requirements for the degree of
Master of Science
2020

Advisory Committee:
Professor Mario Dagenais, Chair
Dr. Behrang Hamadani, Co-chair
Professor Agis Iliadis

© Copyright by
Sai Meghasena Chavali
2020

Acknowledgements

I would like to express my deepest gratitude to my NIST advisor Dr. Behrang Hamadani for giving me the opportunity to work under his guidance and for his unwavering support and encouragement without which this work would not have been realized. I would also like to thank my UMD advisor, Prof. Mario Dagenais, for providing me with valuable feedback and suggestions for my research. I am also grateful to my supervisor Dr. Bill Healy who helped provide the opportunity and resources to make my thesis research possible. Thank you also to Prof. Iliadis for serving on my thesis defense committee.

I would like to extend my gratitude to my coworker, John Roller, for helping me work through challenges in my thesis research. Thank you also to the rest of my coworkers in the NIST Energy and Environment Division for supporting me and for creating a pleasurable work environment.

Finally, I would like to thank my parents for their continual support and encouragement.

Table of Contents

| | |
|--|-----|
| Acknowledgements..... | ii |
| Table of Contents..... | iii |
| Introduction..... | 1 |
| Chapter 1: Background..... | 3 |
| 1.1 Solar Spectrum..... | 3 |
| 1.2 Optical Processes in Solar Cells..... | 7 |
| 1.2.1 Generation..... | 7 |
| 1.2.2 Recombination Mechanisms..... | 8 |
| 1.3 Derivation of Solar Cell I-V Characteristics..... | 10 |
| 1.3.1 Detailed Balance..... | 10 |
| 1.3.2 Key Parameters from an I-V Curve..... | 13 |
| 1.4 Characterizing Solar Cells via Electroluminescence..... | 15 |
| 1.4.1 Reciprocity Theorem..... | 16 |
| 1.5 Fundamental Losses in Solar Cells..... | 18 |
| Chapter 2: Data Acquisition via Hyperspectral Imaging..... | 21 |
| 2.1 What is hyperspectral imaging..... | 21 |
| 2.2 Instrumentation..... | 23 |
| 2.3 Post-processing of Hyperspectral Cube Data..... | 29 |
| 2.4 Calibration of Hyperspectral Cube Data..... | 33 |
| 2.4 Hyperspectral Cube Images for a GaAs Solar Cell..... | 37 |
| Chapter 3: Characterizing Subcell Losses in Multijunction Solar Cells..... | 40 |
| 3.1 Different Multijunction Solar Cells..... | 40 |
| 3.2 Calculation of I-V curves from Electroluminescence Data..... | 40 |
| 3.2.1 Absolute EL spectra with multiple injection current densities..... | 41 |
| 3.2.2 External EL quantum yield y_{extLED} vs. $JLED$ | 44 |
| 3.2.3 External luminescence quantum yield y_{ext} | 46 |
| 3.2.4 I-V curves of three junction solar cells..... | 53 |
| 3.3 Double Diode Model..... | 58 |
| 3.5 Losses from three different solar cells..... | 64 |
| Chapter 4: Conclusions..... | 72 |
| Bibliography..... | 74 |

Introduction

Solar cells are based on semiconductor materials which absorb the electromagnetic radiation from the sun and convert it into electrical energy. The efficiency of a solar cell describes how much of the incident radiation from the sun is converted to electrical energy we can use. The material properties of the semiconductor along with the device structure and other optical factors such as light trapping play an important role in determining the efficiency of the solar cell.

Silicon is the most common material used in solar cells as approximately 90% of the solar cell modules in the industry are based on silicon. This material is widely used because of its abundance on Earth, high efficiency, low cost and long lifetime [1].

There are two main types of silicon used in manufacturing solar cells:

monocrystalline silicon and polycrystalline silicon. Monocrystalline silicon is made up of a single crystal of silicon having an ordered crystal structure. It is this uniformity that makes monocrystalline silicon solar cells extremely efficient but due to a complicated manufacturing process, it is the most expensive type of silicon [2].

Polycrystalline silicon is comprised of multiple crystals of silicon that are melted, cooled and then cut into wafers [3]. The manufacturing process is cheaper and simpler but these cells are less efficient due to their nonuniformity. The highest efficiency of a monocrystalline silicon solar cell is around 27.6% whereas the highest efficiency of a polycrystalline silicon solar cell is around 23.2% [4].

Aside from silicon-based solar cells, thin-film technologies and multijunction cells are other types of solar cells that are used in various manufacturing facilities and have comparable efficiencies. Thin film solar cells are made by depositing one or more

thin layers of semiconductor material, such as cadmium telluride (CdTe) and copper indium gallium diselenide (CIGS), onto a substrate [1, 5]. Currently, the highest efficiency for a thin film solar cell is around 23.2% [4]. As we will see in the next section, the sun emits light spanning a range of wavelengths and the most efficient solar cell will take advantage of this by converting as much of the incident solar radiation to electrical energy as possible. Each semiconductor material has different material properties that affects its efficiency. Multijunction solar cells are comprised of different semiconductor materials stacked on top of each other in order to take advantage of each material's properties and absorb as much of the solar spectrum as possible. The highest efficiency reported for a multijunction solar cell is around 47.1% under high concentration [4].

In this thesis, we will study three different multijunction solar cells and will see how each cell's individual junction material properties determine the overall efficiencies. Through simple electroluminescence measurements and following a series of calculations, we have been able to obtain loss parameters for each junction in a multijunction cell. Such detailed characterization for each junction allows for better understanding of the solar cell performance. Before we discuss these issues in more detail, it is first important to learn about the physics of the solar radiation.

Chapter 1: Background

1.1 Solar Spectrum

The sun emits light spanning the ultraviolet, visible and infrared regions of the electromagnetic spectrum. Solar irradiance is the amount of radiant energy – photons – received from the sun in power per unit area. The solar radiation spectrum is commonly presented as spectral irradiance (units: W/m²/nm) as a function of wavelength (units: nm). In order to get the total solar irradiance in power per unit area (W/m²), the spectral irradiance must be integrated over all the wavelengths. Solar irradiance peaks at visible wavelengths of around 400-700 nm (~550 nm is the peak). Due to the sun's surface temperature of around 5760 K [6], its radiation spectrum can be approximated as that of a black body of the same temperature. A black body emits radiation that is dependent purely on its temperature T . The *spectral photon flux* Φ_{bb} ($E, \mathbf{s}, \theta, \varphi$), is the number of photons with energy in the range E to $E + dE$ emitted through unit area per unit solid angle per unit time at some point \mathbf{s} on the surface of the black body [6]. This expression is given by

$$\Phi_{bb}(E, \mathbf{s}, \theta, \varphi) d\Omega d\mathbf{S} dE = \frac{2}{h^3 c^2} \left(\frac{E^2}{\exp\left(\frac{E}{kT}\right) - 1} \right) d\Omega d\mathbf{S} dE \quad (1.1)$$

where h is Planck's constant, c is the speed of light in vacuum, and k is Boltzmann's constant. In equation 1.1, $d\mathbf{S}$ is the element of surface area around \mathbf{s} and $d\Omega$ is the unit of solid angle around the direction of emission of light (θ, φ). In order to obtain the flux normal to the surface φ_{bb} , the component Φ_{bb} must be integrated over the solid angle and resolved along $d\mathbf{S}$. The expression for φ_{bb} is given in equation 1.2 as follows. Figure 1a shows the relationship between Φ_{bb} and φ_{bb} .

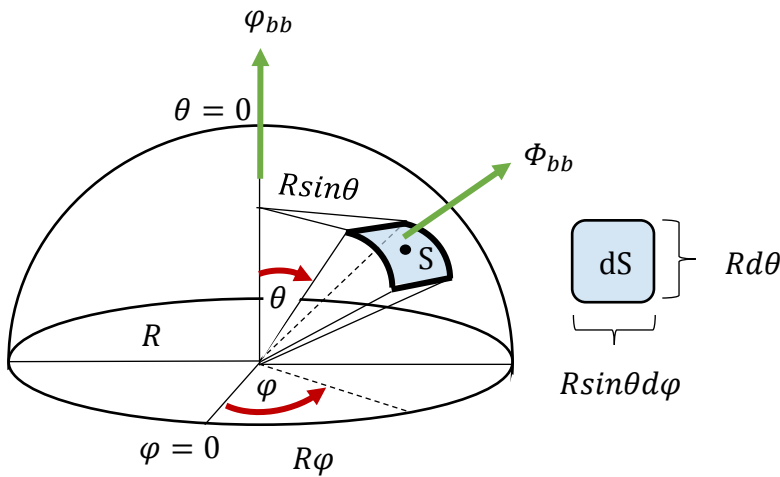
$$\begin{aligned}\varphi_{bb}(E, \mathbf{s})d\mathbf{S}dE &= \int_{\Omega} \beta_s(E, \mathbf{s}, \theta, \varphi) \cdot \cos\theta \, d\Omega d\mathbf{S}dE \\ &= \frac{2F_s}{h^3 c^2} \left(\frac{E^2}{\exp\left(\frac{E}{kT}\right) - 1} \right) d\mathbf{S}dE\end{aligned}\quad (1.2)$$

F_s is the projected solid angle that results from integrating over the appropriate angular range and is given by

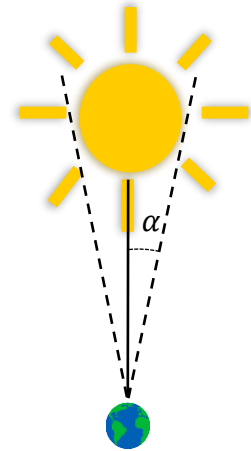
$$F_s = \pi \sin^2 \alpha \quad (1.3)$$

where α is the half angle subtended by the radiating body, the sun, to the point where the flux is measured. If the flux was measured at the surface of the blackbody, the total angular range would be the hemisphere and $F_s = \pi$. For the sun as seen from the Earth as shown in figure 1b, $\alpha = 0.26^\circ$. The argument \mathbf{s} can be omitted from φ_{bb} if the temperature at the surface of the black body is uniform. In this case, the expression for φ_{bb} can be written as

$$\varphi_{bb}(E) = \frac{2F_s}{h^3 c^2} \left(\frac{E^2}{\exp\left(\frac{E}{kT}\right) - 1} \right) \quad (1.4)$$



a) Geometry used to obtain solid angle $d\Omega$



b) Illustration showing half angle of sun as seen from Earth

Figure 1: Relationship between Φ_{bb} and φ_{bb} and illustration of half angle α

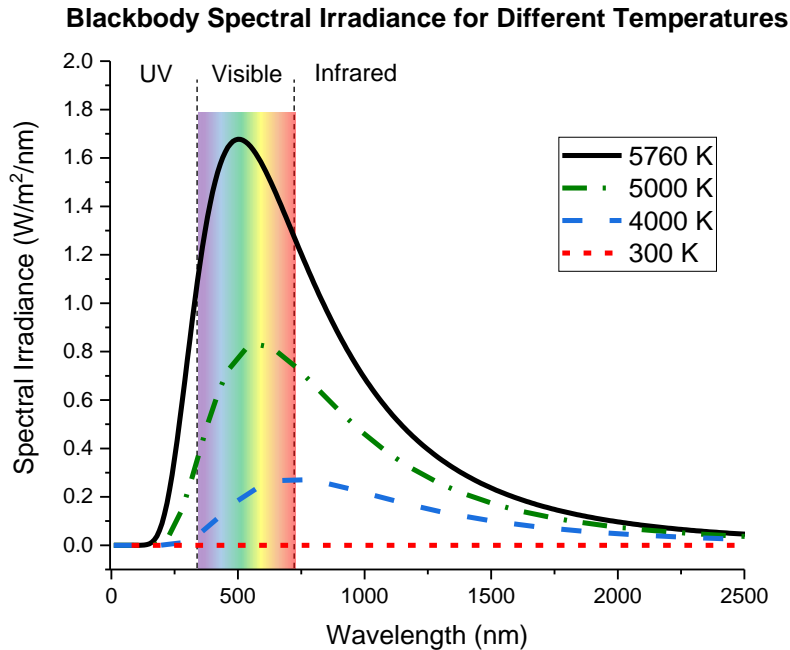


*Figure 2: Blackbody spectral irradiance for different temperatures ***computed with half angle of sun. Not computed for pure blackbody, modified by factor of half angle of sun in sky reported to be 0.26 degrees*

Figure 2 is a plot of the blackbody spectral irradiance for 5760 K, 5000 K, 4000 K, and 300 K. As shown in this plot, the spectral irradiance is highest corresponding to the temperature of the sun of 5760 K and falls within the visible range of the electromagnetic spectrum. Observe that around room temperature of 300K, there is little to no blackbody spectral irradiance in the range plotted here. It is important to note that this plot is the amount of blackbody radiation as seen by someone on earth. It is not computed for a blackbody on the surface but rather modified by a factor of half angle of sun in sky which is reported to be 0.26 degrees. The blackbody emission at the sun's temperature of 5760 K falls within the range of visible light. As the temperature of the blackbody decreases, the peak of the emission shifts more into the IR range of wavelengths and the intensity of irradiance also decreases because the

emission is exponentially dependent on the inverse of the temperature. The colder the blackbody, the less emission.

When we take $\alpha = 0.26^\circ$, the expression for φ_{bb} represents the spectral photon flux density of the sun as measured by someone on earth and represents the number of photons emitted from the sun per unit area per energy. The solar irradiance or emitted power density is related to the spectral photon density by

$$L(E) = E\varphi_{bb}(E) \quad (1.5)$$

The total solar irradiance is obtained by integrating $L(E)$ over all E . The power density at the sun's surface is 62 MW/m² but the solar irradiance as observed just outside the Earth's atmosphere is reduced to 1353 W/m² due to the Earth's great distance from the sun [6]. As the sunlight passes through the atmosphere, some of the light is absorbed and scattered by particles in the atmosphere so that the solar radiation spectrum reaching the surface of the Earth is further attenuated. The 'Air Mass' is a factor quantifying the absorption in the atmosphere and how it affects the distribution and intensity of the solar spectrum reaching the Earth's surface. The 'Air Mass' number is given by

$$Air\ Mass = \frac{1}{\cos \theta} \quad (1.6)$$

Where θ is the angle of incidence of the sunlight ($\theta = 0$ when the sun is directly overhead). Air Mass 1.5 or AM1.5 ($\theta = 48.2^\circ$) is a widely used standard spectrum normalized to an integrated irradiance of 1000 W/m². Figure 3 illustrates the angle of incidence of sunlight for AM0 and AM1.5. The solar radiation spectrum reaching the Earth's surface has a diffuse or indirect component as well meaning the light is incident from all angles rather than directly from the sun. This diffuse component

accounts for up to 15% of the light reaching the Earth's surface but can be larger at high altitudes or in areas with more cloud cover [7]-[9]. The air mass number is also defined by whether the diffuse component is included. The AM1.5g (global) spectrum includes the diffuse component whereas the AM1.5d (direct) does not. A plot of the AM0, AM1.5g and AM1.5d spectrums is shown in figure 4.

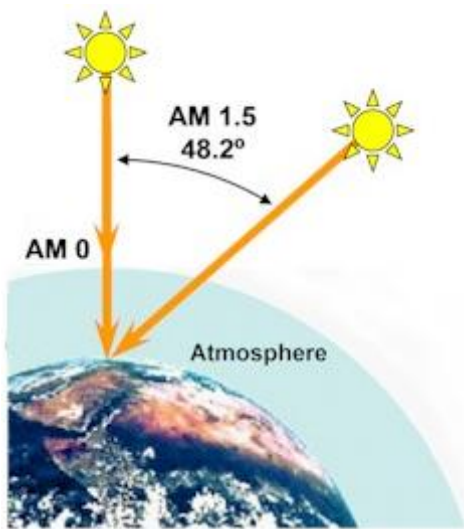


Figure 3: Illustration of angle of incidence of sunlight for AM0 and AM1.5 Adapted from [10]

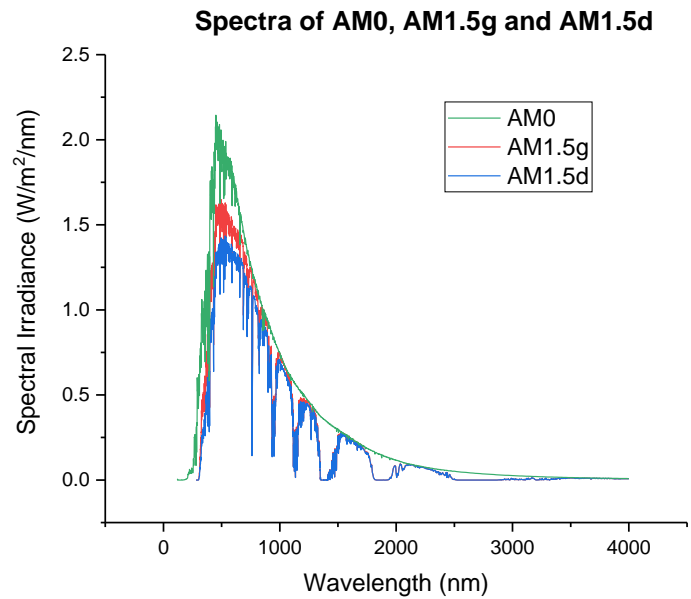


Figure 4: Plot of AM0, AM1.5d and AM1.5g

1.2 Optical Processes in Solar Cells

1.2.1 Generation

In order to harness the sun's energy, the light energy must be converted into electrical energy that can be used. In a solar cell, absorption of sunlight occurs when the incident light excites electrons from the valence band to the conduction band, generating electron-hole pairs (EHPs). The energy of these excited electrons generates a potential difference or voltage and as a result, a current is supplied into an electric circuit. In an ideal solar cell and in the absence of mid-gap defects, photons

from the incident light are only absorbed if they have energy equal to or greater than the band gap energy of the semiconductor. If the photons have energy less than the band gap, the photons will be transmitted through the material. This is the reason why pure silicon is transparent at wavelengths greater than 1200 nm.

In direct band gap semiconductors like GaInP and GaAs, the crystal momentum is the same for electrons and holes in the conduction band and valence band respectively [11]-[12]. Photons are easily absorbed in such semiconductors because no change in momentum is needed for an electron to be excited to the conduction band. In an indirect band gap semiconductor such as Ge, the valence band maximum occurs at a different crystal momentum from the conduction band minimum. In order to conserve electron momentum during the photon absorption process, there must be a phonon involved. Phonons represent lattice vibrations in a semiconductor and since the lattice vibrations are random, the probability of encountering a phonon of the right momentum for absorption is very low. Therefore, photon absorption is very low in indirect band gap semiconductors and as a result, thicker layers and photonic engineering are needed to absorb all the incoming photons [7].

1.2.2 Recombination Mechanisms

Whether charge carriers, i.e., electrons and holes are generated via illumination or via injection of current, the concentration of holes and electrons will eventually tend toward their equilibrium levels. Recombination is the process of an electron losing energy and thermalizing back to the valence band. This section will discuss the three main types of recombination: Radiative, Shockley-Read-Hall and Auger recombination [13]–[15]. In equations 1.7 through 1.9 below, n represents the

electron concentration, p represents the hole concentration and n_i represents the intrinsic carrier concentration.

Radiative

Radiative or band-to-band recombination is the inverse of the EHP generation process in semiconductors and is more efficient in direct bandgap semiconductors. In this recombination, an electron in the conduction band directly combines with a hole in the valence band and releases a photon whose energy E_{ph} is approximately equal to the energy of the bandgap E_g . The net recombination rate follows equation 1.7 where B is a radiative recombination constant.

$$U_{rad} = B(pn - n_i^2) \quad (1.7)$$

Shockley-Read-Hall

Shockley-Read-Hall (SRH) recombination is a two-step process that occurs through lattice defects, or traps in the semiconductor. An electron from the conduction band falls into a trap with energy E_T . From this trap energy level, the electron can make a second transition to an empty state in the valence band, recombining with a hole. It is also possible for the recombination to occur at the energy level E_T if a hole from the valence band is excited to the trap energy level before the electron is re-emitted to the conduction band. The net recombination rate follows equation 1.8 where $\tau_{SRH,n}$ and $\tau_{SRH,p}$ represent the carrier lifetimes for the electrons and holes respectively and $E_i = E_g/2$.

$$U_{SRH} = \frac{pn - n_i^2}{\tau_{SRH,n} \left(p + n_i e^{\frac{E_i - E_T}{kT}} \right) + \tau_{SRH,p} \left(n + n_i e^{\frac{E_T - E_i}{kT}} \right)} \quad (1.8)$$

Auger

Auger recombination is a three-carrier process similar to radiative recombination but instead of the energy being emitted as a photon, the energy is given to another carrier either in the conduction band or the valance band. This third carrier then thermalizes back to its original energy, giving up the extra energy to phonons and ultimately as heat to the lattice. Auger recombination is the inverse process to impact ionization, where a high energy electron collides with an atom in the crystal, breaking the bond and creating an electron-hole pair. The net recombination rate follows equation 1.9 where C_n and C_p are parameters of the material for low-injection.

$$U_{Auger} = (C_n n + C_p p)(pn - n_i^2) \quad (1.9)$$

Figure 5 below illustrates the three recombination processes in semiconductors.

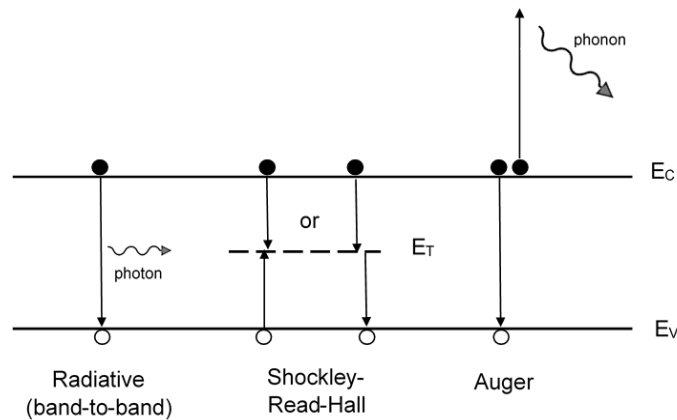


Figure 5: Recombination Processes in Semiconductors

1.3 Derivation of Solar Cell I-V Characteristics

1.3.1 Detailed Balance

The detailed balance limit also known as the Shockley-Queisser limit states that at thermal equilibrium, there must be a balance between the incoming photons from the sun and the outgoing photons from recombination to obtain a maximum efficiency

and current-voltage (I-V) characteristic of a solar cell. This principle is based a few assumptions [16]-[18]:

- (i) All photons with energy E_{ph} greater than the bandgap E_g will be absorbed and will generate electron-hole pairs (EHPs)
- (ii) There is perfect collection of carriers – leading to infinite mobility
- (iii) Radiative recombination is the only allowed mechanism for recombination

These assumptions will be used to derive the short-circuit current or photocurrent and ultimately to derive the I-V characteristic of a solar cell.

Photocurrent J_{sc}

The photocurrent density J_{sc} under illumination is due to the net absorbed flux from the sun ϕ_{sun} and is defined by equation 1.10.

$$J_{sc} = q \int_0^{\infty} a(E) \phi_{sun}(E) dE = q \int_{E_g}^{\infty} \phi_{sun}(E) dE \quad (1.10)$$

Where q is the elementary charge and $a(E)$ is the absorptance. Every photon is absorbed above the bandgap so the absorptance is assumed to be zero below and unity above the bandgap energy E_g .

Dark Current J_{dark}

When a solar cell is in thermal equilibrium with the ambient, i.e. when the cell is in the dark, every photon absorption event must be balanced by the inverse process of a photon emission event. Any contradiction of this assumption of thermal equilibrium means that there is a net flow of energy. When a bias is applied across the solar cell, the device is no longer in equilibrium. As a result of the applied bias, there is a non-zero chemical potential $\Delta\mu$ equal to the quasi-Fermi level splitting at the position

where radiation is emitted. Assuming that $\Delta\mu$ is constant everywhere and equal to the product qV , the emitted photon flux ϕ under the applied bias voltage V is given as shown in equation 1.11.

$$\phi[V, E] = \frac{2\pi E^2}{h^3 c^2} \frac{a(E)}{\exp\left(\frac{E - qV}{kT}\right) - 1} \quad (1.11)$$

Where h is Planck's constant, c is the speed of light in vacuum, k is Boltzmann's constant and T is temperature. This equation is very similar in form to equation 1.4 because it is also a photon flux density but due to an applied bias voltage. Equation 1.11 can be simplified to

$$\phi[V, E] = a(E)\phi_{bb}(E) \exp\left(\frac{qV}{kT}\right) \quad (1.12)$$

When a bias is applied to a solar cell, recombination is the only way for photon emission to occur and since radiative recombination is one of the assumptions of the detailed balance limit, the emitted photon flux described in equation 1.11 must be due to a recombination current J_{rec} . Therefore, the entire recombination current $J_{rec} = q\Phi$ where Φ is the integration of $\phi[V, E]$ over all energies [16]-[18]. The dark current is the current which flows through the solar cell when a bias is applied in the dark and under these conditions, the total current is given by

$$J_{dark} = J_{0,rad} \left(e^{\frac{qV}{kT}} - 1 \right) \quad (1.13)$$

Where $J_{0,rad}$ is the radiative saturation current density is given by

$$J_{0,rad} = q\Phi(0) = q \int a(E)\phi_{bb}(E)dE = q \int_{E_g}^{\infty} \phi_{bb}(E)dE \quad (1.14)$$

Derivation of I-V Characteristic

In order to get the overall current-voltage (I-V) characteristic of the solar cell, the dark current J_{dark} must be subtracted from the photocurrent J_{sc} to get the net current density J [19].

$$J = J_{\text{sc}} - J_{\text{dark}} = J_{\text{sc}} - J_{0,\text{rad}}(e^{\frac{qV}{kT}} - 1) \quad (1.15)$$

From this equation, it can be seen that the maximum voltage generated due to illumination is when the net current density J is equal to zero. Having a net current density of zero means that the solar cell is under open circuit conditions and therefore the maximum voltage is referred to as the open-circuit voltage. Setting $J = 0$ and solving for V , we obtain the radiative limit for the open-circuit voltage V_{oc} as shown in equation 1.16. This is known as the radiative limit because of the detailed balance assumption that radiative recombination is the only allowed mechanism for recombination.

$$V_{\text{oc,rad}} = \frac{kT}{q} \ln \left(\frac{J_{\text{sc}}}{J_{0,\text{rad}}} + 1 \right) \quad (1.16)$$

1.3.2 Key Parameters from an I-V Curve

Short-circuit current and open-circuit voltage

The *short-circuit current* I_{sc} and the *open-circuit voltage* V_{oc} are both characteristics of the solar cell that can be seen from an I-V curve. The short-circuit current is the maximum current that can be drawn from the device when the voltage across the device is zero. Sometimes, we divide the current, I , by the solar cell area, A , to get the

current density, $J = I/A$ and make J-V plots. The open-circuit voltage is the maximum voltage available from the solar cell when the net current density is equal to zero.

Fill Factor

The *power density (power generated per unit area of the cell)* for a solar cell is given by equation 1.17 below.

$$P = JV \tag{1.17}$$

The short-circuit current and the open-circuit voltage are the maximum current and voltage from the solar cell but the power density at these points is zero. The power density is a maximum at the solar cell’s *maximum power point* which occurs at a voltage V_m and current density J_m where the product of current and voltage produce a local maxima. The fill factor (FF) is a ratio of the maximum power of a solar cell to the product of J_{sc} and V_{oc} given by equation 1.18 and describes the “squareness” of the I-V curve. The less “square” the I-V curve, the lower the maximum power point. In other words, bending at the knee of the I-V curve means a lower fill factor.

$$FF = \frac{J_m V_m}{J_{sc} V_{oc}} \tag{1.18}$$

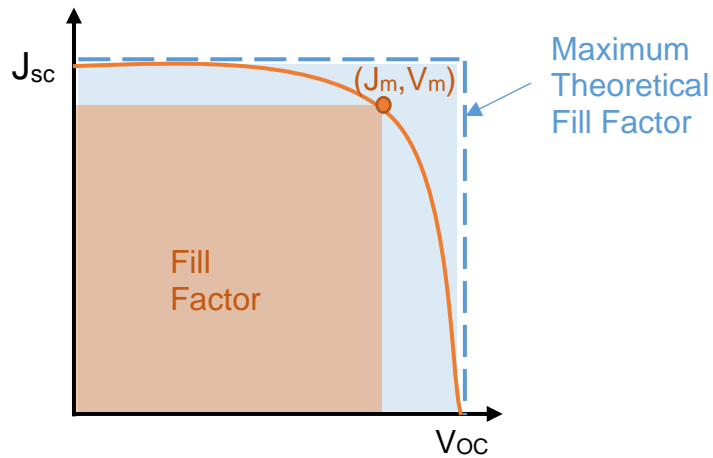


Figure 6: Fill factor of a solar cell

The power conversion Efficiency

The power conversion efficiency (PCE) of a solar cell η is the ratio of the power density at maximum power point to the incident power density P_{in} from the source of illumination. The efficiency η is therefore given by:

$$\eta = \frac{J_{sc}V_{oc}FF}{P_{in}} \quad (1.19)$$

The incident power density P_{in} is the power density coming from the sun and is slightly different for different illumination conditions such as AM0 and AM1.5. The J_{sc} , V_{oc} , FF and η are the main characteristics describing the performance of a solar cell.

1.4 Characterizing Solar Cells via Electroluminescence

Photon absorption excites carriers to higher energy levels and leads to the creation of the excess electron-hole pairs. These excess electron-hole pairs eventually recombine and thermalize to their equilibrium states. In direct bandgap materials like GaAs, the recombination process results in an emission of a photon and is known as radiative recombination as discussed in previous sections. If the carriers are excited by photon absorption, the resulting luminescence from recombination is known as photoluminescence. If the carriers are excited by applying an electric current to the solar cell, the process of photon emission from recombination is known as electroluminescence. An example of devices that exhibit this phenomenon is the light emitting diode or LED where electric energy is converted directly into light energy. It is important to notice that electroluminescence, or EL, is the reciprocal process to the conventional operation of a solar cell in which light energy is converted to electric

energy. This reciprocity is one of the fundamental concepts for the research presented in this thesis.

1.4.1 Reciprocity Theorem

The reciprocity theorem relates a solar cell's carrier collection properties to its electroluminescence emission [20]-[21]. The electroluminescence intensity φ_{em} in units $\frac{\text{photons}}{\text{m}^2 \cdot \text{s} \cdot \text{eV}}$ is given by

$$\varphi_{em}(E, V) = EQE(E)\varphi_{bb}(E) \exp\left(\frac{qV}{kT}\right) \quad (1.20)$$

In equation 1.20 above, kT/q is the thermal voltage, V is the internal junction voltage, E is the photon energy and EQE is the photovoltaic external quantum efficiency.

Notice that the terms in the reciprocity theorem can be expressed in terms of current densities so that an equation for the radiative emission current J_{em} is obtained.

$$q \int_0^{\infty} \varphi_{em}(E, V) dE = \left[q \int_0^{\infty} EQE(E)\varphi_{bb}(E) dE \right] \left[\exp\left(\frac{qV}{kT}\right) \right] \quad (1.21)$$

$$J_{em} = J_{em,0} \exp\left(\frac{qV}{kT}\right) \quad (1.22)$$

Notice that $J_{em,0}$ and $J_{0,rad}$ from equation 1.15 are the same. Following similar steps as in equation 1.16, the radiative emission current J_{em} must be subtracted from the photogenerated current J_{sc} to get the net current density.

$$J = J_{sc} - J_{em} = J_{sc} - J_{em,0} \exp\left(\frac{qV}{kT}\right) \quad (1.23)$$

It is from this expression that the radiative limit for the open circuit voltage $V_{oc,rad}$ can be derived once again and it can be seen that it follows from the photovoltaic quantum efficiency.

$$V_{oc,rad} = \frac{kT}{q} \ln \left(\frac{J_{sc}}{J_{em,0}} \right) \approx \frac{kT}{q} \ln \left(\frac{q \int_0^\infty EQE(E) \phi_{sun}(E) dE}{q \int_0^\infty EQE(E) \phi_{bb}(E) dE} \right) \quad (1.24)$$

As mentioned previously, $V_{oc,rad}$ is the maximum voltage available from the solar cell and it is the ideal case because it is assumed that only radiative recombination is present. However, in a non-ideal scenario, there will be non-radiative recombination as well which contributes to a loss term [22]-[29]. In order to quantify this loss, it is first important to define the external luminescence quantum yield y_{ext} which relates the radiative emission current with the non-radiative recombination current J_{nr} . The external luminescence quantum efficiency represents the number of external photons produced per excited carrier.

$$y_{ext} = \frac{J_{em}}{J_{em} + J_{nr}} = \frac{J_{em,0} \exp\left(\frac{qV}{kT}\right)}{J_{em} + J_{nr}} \quad (1.25)$$

In equation 1.25, $J_{em} + J_{nr}$ represents the current injected in the dark by the applied voltage bias V . In open circuit condition, $J_{em} + J_{nr} = J_{sc}$ since the total current must equal zero (i.e. $(J_{em} + J_{nr}) - J_{sc} = 0$). Solving for the V_{oc} yields the expression shown in equation 1.26.

$$V_{oc} = \frac{kT}{q} \ln \left(\frac{J_{sc} y_{ext}}{J_{em,0}} \right) \quad (1.26)$$

The loss term due to nonradiative recombination can be seen from the difference of the radiative limit for V_{oc} in equation 1.24 and the real V_{oc} given in equation 1.26.

$$\Delta V_{oc} = V_{oc,rad} - V_{oc} = \frac{kT}{q} \ln \left(\frac{J_{sc}}{J_{em,0}} \right) - \frac{kT}{q} \ln \left(\frac{J_{sc} y_{ext}}{J_{em,0}} \right) = -\frac{kT}{q} \ln(y_{ext}) \quad (1.27)$$

Note that the negative sign in front of the term comes from the fact that $y_{ext} < 1$ with the presence of J_{nr} and as a result the $\ln(y_{ext})$ will be negative. Therefore, the ideal

open circuit voltage or radiative limit is penalized by poor external luminescence quantum efficiency. The efficient extraction of photons or light without nonradiative recombination yields high voltages.

$$V_{oc} = V_{oc,ideal} - \frac{kT}{q} \ln(y_{ext}) \quad (1.28)$$

The loss due to nonradiative recombination is just one of the fundamental losses present in solar cells. The next section will provide an overview of these losses.

1.5 Fundamental Losses in Solar Cells

There are six main losses in solar cells: radiative emission or radiative recombination, nonradiative recombination, luminescence coupling, thermalization loss, transmission loss, and junction loss [30]-[35]. Figure 7 below illustrates these loss processes.

Radiative and Nonradiative recombination

Radiative emission occurs when an excited carrier recombines and emits a photon.

Nonradiative recombination occurs when an excited carrier recombines with a phonon emission which is lost as heat to the lattice.

Luminescence coupling

This loss is more prevalent in multijunction solar cells. In a multijunction solar cell such as a triple junction cell, there are three layers of semiconductors stacked on top of each other in order of descending band gap energies. For a photon to be absorbed, it has to have energy greater than the bandgap E_g of the semiconductor. When photons are absorbed and recombine radiatively, photons are emitted in all directions. Some of these photons are emitted out of the device and this is known as radiative recombination. However, some of these emitted photons *couple* into the junction

below and this process is known as luminescence coupling [36, 37]. This loss is shown in figure 7b below.

Thermalization loss

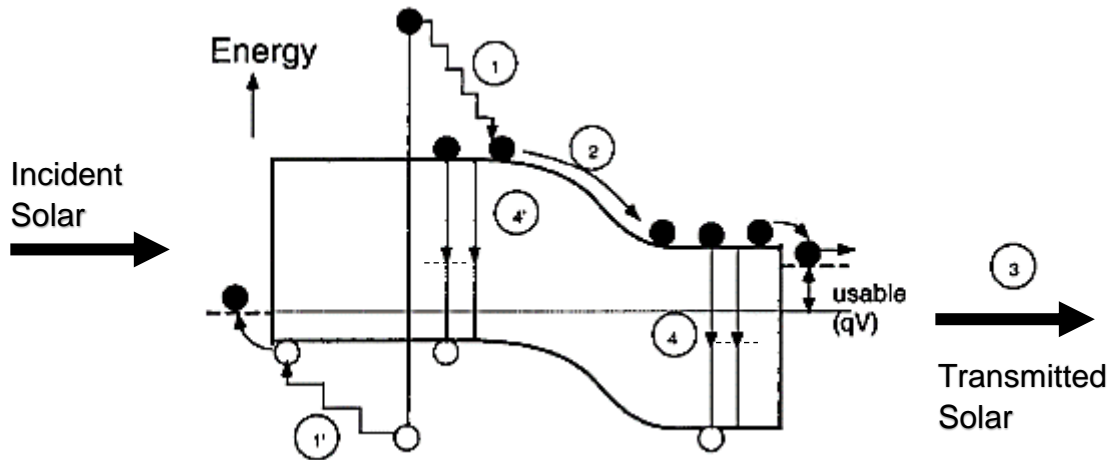
When solar radiation is absorbed, some of the generated carriers are excited to an energy greater than the band gap energy. The process of these excited carriers thermally relaxing to the edge of the band gap energy within the conduction band is known as thermalization loss.

Transmission loss

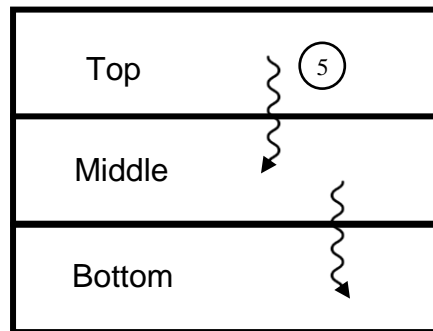
Incident solar radiation below the band gap of the device is not absorbed, but rather transmitted through the device. This is known as transmission loss.

Junction loss

In the operation of a solar cell, excited carriers are fed into an electric circuit so that the power can be harvested. However, some of the excited carriers lose potential energy as they travel to the junction contacts and this is known as junction loss.



a) Standard p-n junction; figure adapted from [32]



b) Multijunction solar cell

Figure 7: Illustrations of losses in solar cells: (1) Thermalization loss; (2) Junction loss; (3) Transmission loss; (4) Radiative and nonradiative recombination; (5) Luminescence coupling

The research presented in this paper will focus on verifying a method to extract these losses via absolute electroluminescence measurements. The instrumentation used to collect electroluminescence data is highlighted in the next chapter.

Chapter 2: Data Acquisition via Hyperspectral Imaging

2.1 What is hyperspectral imaging

In order to understand hyperspectral imaging, it is first necessary to understand spectroscopy. Spectroscopy is the study of interaction between materials and electromagnetic radiation and a spectrometer is an instrument that splits the incoming light into a spectrum of different wavelengths. Each material has a unique spectrum, so we are able to identify materials based on spectral signatures. Hyperspectral imaging is a technique that combines spectroscopy and imaging to obtain a spectrum for each pixel in the image of a target. The result of hyperspectral imaging is a 3-D data cube. For example, digital and smartphone cameras divide the spectrum of the target into three wavelength bands – red, green and blue (RGB) – to match the human vision. On the other hand, hyperspectral imaging divides the spectrum of the target into many more bands covering the visible and near-infrared range. It is important to note that hyperspectral imaging which refers to the continuous measurement of narrow spectral bands differs from multispectral imaging which measures a discrete number of spaced spectral bands.

There are two main ways a hyperspectral imager can scan an image: spatial scanning which reads images over time (i.e. push broom and whisk broom scanners) and spectral scanning which obtains images of a target at different wavelengths. In spatial scanning such as push broom scanning, the image is analyzed in lines by projecting the image through a slit. In a whisk broom scanner, a point-shaped aperture is used to scan the image instead of a slit. In spectral scanning, each 2-D (x,y) output obtained from the hyperspectral data cube represents a monochromatic image where the x and y dimensions provide spatial information of the sample and the z dimension represents the wavelength. The object is scanned for each wavelength through different settings of the filter while the stage remains stationary. The hyperspectral imager discussed in this paper follows spectral scanning and is based on an optical tunable filter which will be detailed in future sections. Figure 8 below shows the difference between the different types of hyperspectral imagers.

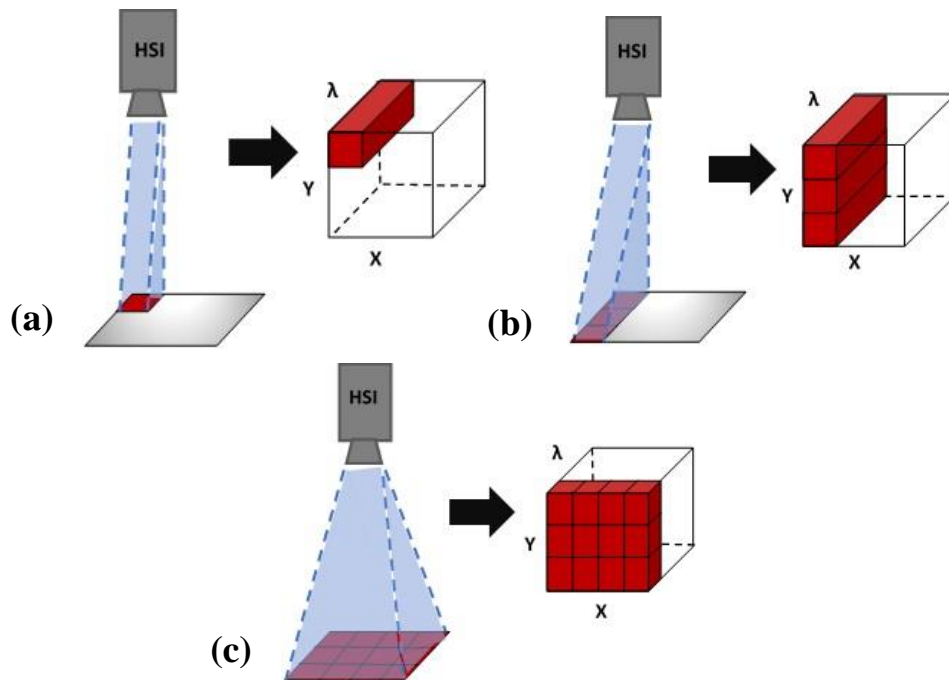


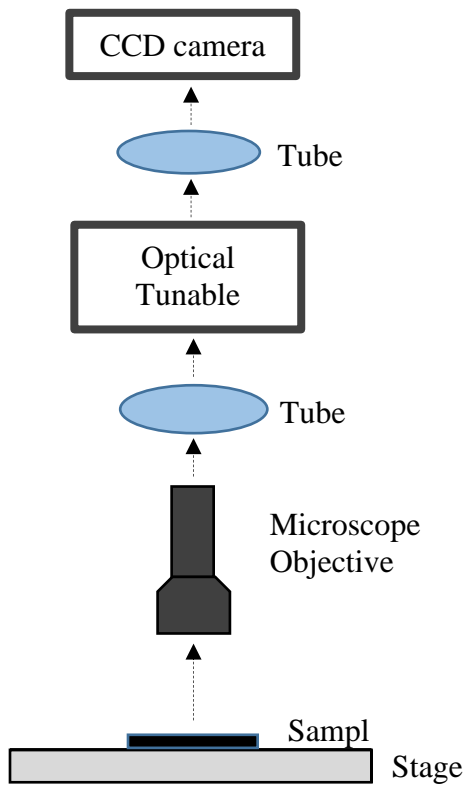
Figure 8: Different types of hyperspectral imagers. (a) whisk broom, (b) push broom, (c) spectral

There are several applications of hyperspectral imaging. For example, in food processing, it is used to detect bruising under avocado skin early on and predict ripeness. It has also been used to detect inhomogeneities in samples such as detecting plastic mixed with rice. In optometry, such imaging is used for the diagnosis of retinopathy and macular edema before damage to eye occurs. In farming, it is used to monitor the growth and health of crops. The application of hyperspectral imaging that will be discussed in this paper is characterization of solar cells using electroluminescence but it is first necessary to learn more about the instrumentation used.

2.2 Instrumentation

The hyperspectral imager used for our data acquisition is the GRAND-EOSTM from Photon etc. This imager has a wide-field imaging platform with both micro- and macro-imaging modalities and with a spectral range from 400 to 1700 nm [38]. As mentioned above, this hyperspectral imager follows spectral scanning which consists of measuring the intensity of light for each pixel at a certain wavelength for all wavelengths in the range of interest. Figure 9a below shows the optical path of the hyperspectral imager and figure 9b shows a photo of the GRAND-EOSTM. The light emitted from the solar cell is collimated by the microscope objective and is then projected by a tube lens onto an optical tunable filter which is used to select a single wavelength. Finally, the light is then focused on to a Charge-Coupled Device (CCD) camera so that a monochromatic image can be formed [39].

(a)



(b)

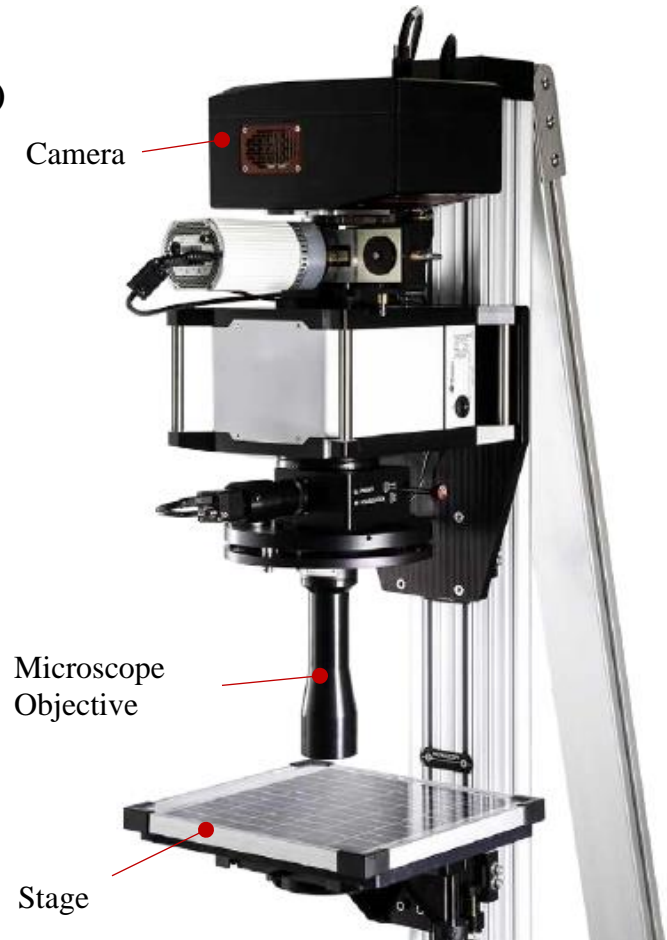


Figure 9: (a) Optical path of hyperspectral imager, (b) GRAND-EOSTM photograph [38]

The Bragg Tunable Filter

The core technology for Photon etc.'s global hyperspectral imager is a Bragg Tunable Filter based on Volume Bragg Gratings (VBG). A VBG is made of a photo-thermo-reflective (PTR) glass (i.e. silver halide) which is exposed to an interference pattern from ultra-violet laser radiation at around 325 nm [40]. When the PTR glass is exposed to this interference pattern, a variation in charge density is generated across the material allowing for modulation of the PTR's refractive index [40]. This modulation can be oriented to either transmit or reflect the incident beam as shown in figure 10. VBGs can be described in terms of the refractive index of the PTR glass n_0 , the period Λ of the grating, the angle θ between the incident beam and the normal of the entrance surface \vec{N} , and the inclination of the Bragg planes which is the angle φ between the normal \vec{N} and the grating vector \vec{K}_g [40]. In the following section, VBG may also be referred to as Bragg grating.

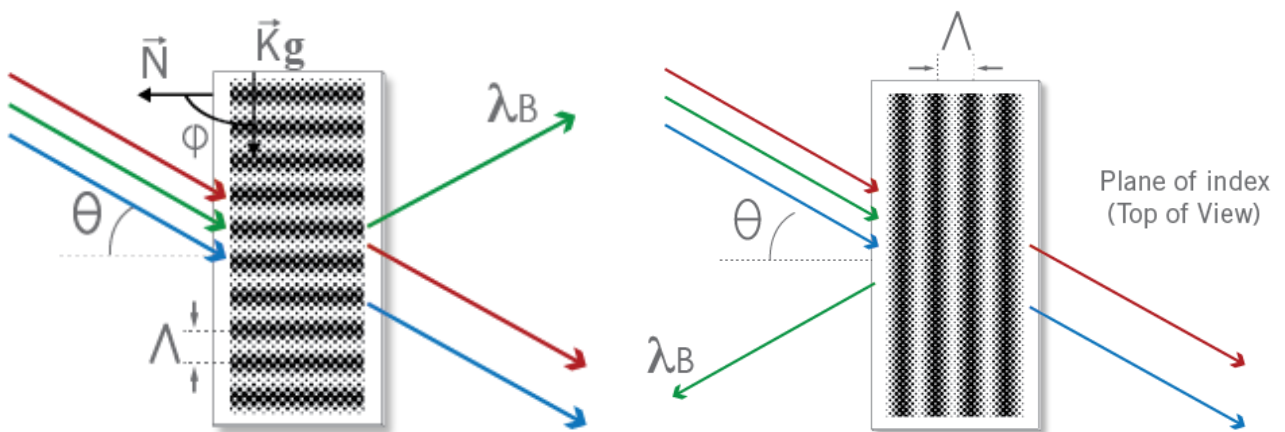


Figure 10: (a) Transmission grating, (b) Reflection grating Adapted from [41]

Only a small portion of the incident polychromatic light is diffracted by the VBG. The wavelength which will be diffracted depends on whether Bragg's condition is satisfied. Bragg's law for a VBG is given as follows where λ_B is the diffracted wavelength [41]:

$$\lambda_B = 2n_0\Lambda \cos(\theta + \varphi) \quad (2.1)$$

As shown in figure 10 above for transmission gratings, the Bragg planes are perpendicular to the entrance surface which means that $\varphi = \pi/2$ and Bragg's law becomes:

$$\lambda_B = 2n_0\Lambda \sin(\theta) \quad (2.2)$$

For reflection gratings, the Bragg planes are parallel to the entrance surface which means $\varphi = 0$ and the Bragg condition becomes:

$$\lambda_B = 2n_0\Lambda \cos(\theta) \quad (2.3)$$

As shown by equations 2.2 and 2.3 above, the diffracted wavelength is dependent on the angle θ of the incident beam. The angle θ can be adjusted so that multiple wavelengths can be imaged. If the incident beam does not meet Bragg's condition, it is not diffracted and simply passes through the grating.

Figure 11 shows the diffraction efficiency spectrum of a transmission Bragg grating shown in figure 9a. The peak, which is centered around 632 nm, has a Full Width at Half Maximum (FWHM) equal to 1.8 nm. In this spectrum, we see that the output of a VBG is dispersive because even though only a narrow band of wavelengths is diffracted, there is still some transmission at other wavelengths in the form of side lobes. The VBG attenuates these side lobes to very low levels [41].

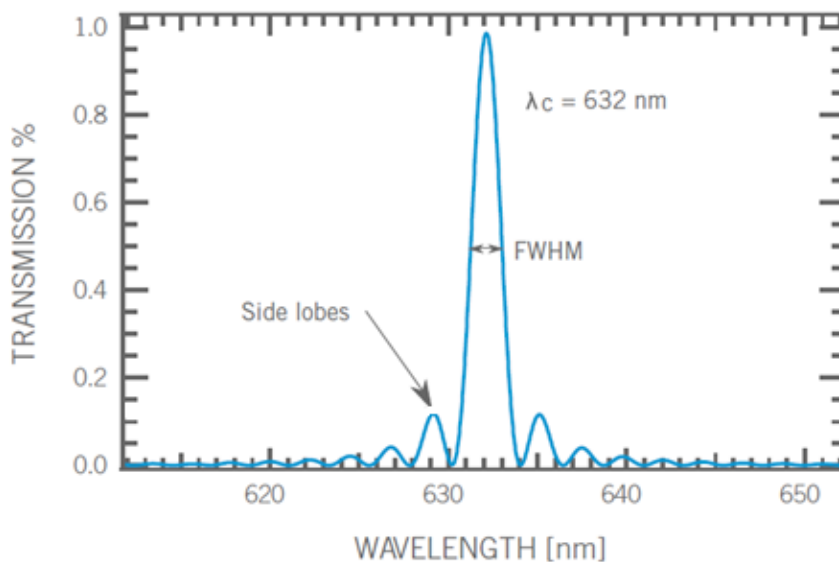


Figure 11: Diffraction efficiency spectrum [40]

As explained above, the output of a Bragg grating is dispersive so the beam needs to be passed through the VBG for a second time in order to account for this dispersion and achieve a reduced bandwidth for the filtered optical signal [42]. As shown in figure 12 below, the corner cube reflects the beam from the first pass of the VBG into another VBG where the output is the filtered optical signal λ_B . This output is then focused onto a CCD camera where it is imaged.

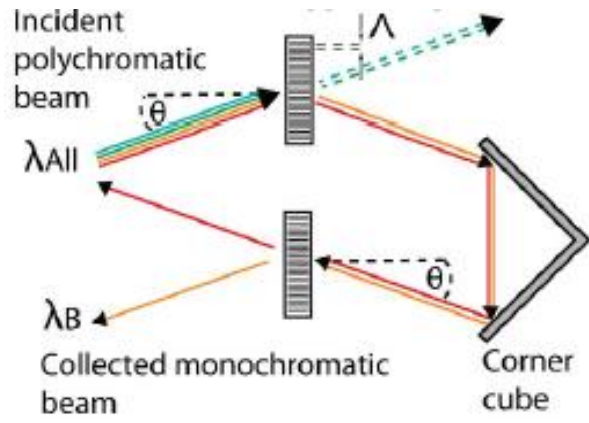


Figure 12: Schematic of Volume Bragg Grating Adapted from [42]

By taking advantage of VBGs' ability to obtain a small band of wavelengths from a polychromatic input, the Bragg Tunable Filter is continuously tunable meaning it can be tuned to select a wide range of wavelengths. Figure 13 below shows the designs for the transmission and reflection imaging Bragg Tunable Filter [43, 44].

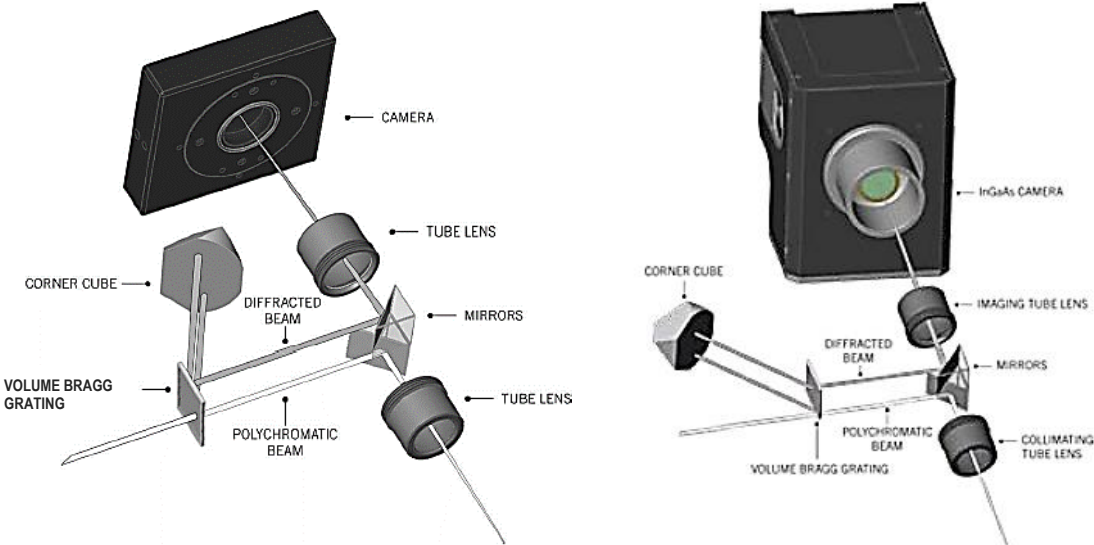


Figure 13: Bragg Tunable Filter using (a) Transmission grating, (b) Reflection grating Adapted from [43, 44]

The input polychromatic beam is focused by the tube lens onto the VBG and after the second pass through the volume hologram, the diffracted beam is focused by another

tube lens onto the CCD camera where it is imaged. The corner cube and the VBG are positioned on rotation stages so that the angle θ can be easily adjusted and the diffracted wavelength can be tuned. An image of the sample is obtained for every wavelength in the desired scanning range.

2.3 Post-processing of Hyperspectral Cube Data

After a hyperspectral cube is taken, some postprocessing needs to be completed before the data is used for analysis. Postprocessing includes dark subtraction, registration correction and wavelength rectification.

Dark Subtraction

We used the hyperspectral imager to look at the luminescence response of a solar cell when a voltage is applied. A “dark” hyperspectral cube is taken first so that it can be subtracted from our “light” data cubes. “Light” refers to the condition where a voltage is applied across the solar cell, resulting in luminescence from the surface of the cell and “dark” refers to the condition where there is no applied voltage across the cell. Subtracting the dark cube allows us to eliminate noise in our data for a more accurate visualization.

Registration Correction

Registration correction corrects for any translation and dilation between the images in the cube that may occur with a change in wavelength and wavelength rectification, which is discussed in detail below, corrects for the gradient in wavelength that arises from imaging [45].

Wavelength Rectification

The image produced on the CCD camera is a sum of point sources originating from different positions of the solar cell as seen by the microscope objective. Each point source on the cell produces a collimated beam with a different incident angle on the VBG. Therefore, the angular selectivity of the grating results in a gradient in wavelength across the image as shown in figure 14a and the image produced on the CCD camera consists of vertical lines each with a specific wavelength [43]. In order to obtain a monochromatic image, one must scan through a range of wavelengths to obtain the wavelength of interest for each image. This reconstruction is done using the wavelength rectification feature in the Photon etc. software.

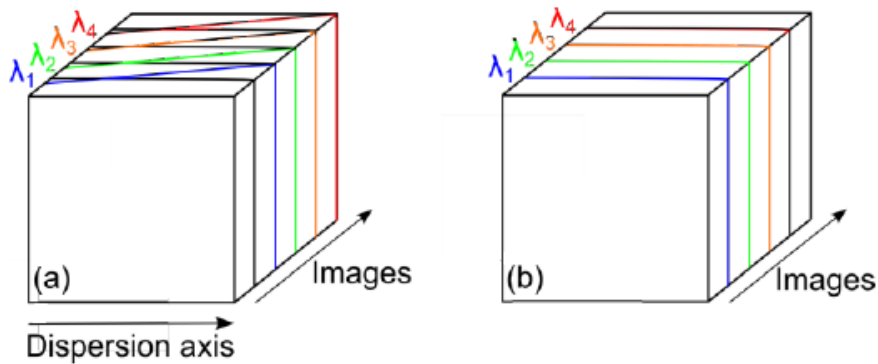


Figure 14: (a) Gradient in wavelength, (b) After reconstruction [44]

Hyperspectral Data Cube

Figure 15 below shows a hyperspectral image for a GaAs solar cell at 870 nm after all post-processing has been completed in the imaging analysis software. The image shows a segment of a larger piece of cell where some variations in the EL signal plus a few “hot spots” are observed.

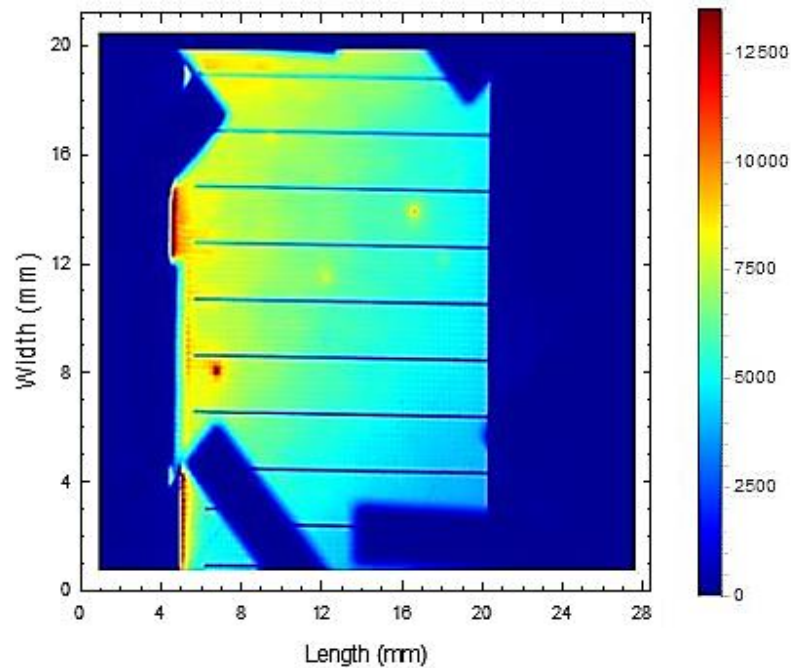


Figure 15: Hyperspectral Image at 870 nm for a GaAs cell

The scalebar shows the relative intensity of the signal in “net counts” with the color blue representing low to zero counts and color red representing areas of highest counts or luminescence. In particular, the left side of the image where current is injected into the cell appears to show a brighter EL intensity than the right side. This is likely due to the latter series resistance of the material. Also of particular interest are localized regions of higher signal such as the large red spots on the left side and a few weaker, yellow spots at other locations. Since recombination via defects is

usually associated with “cold spots”, i.e., areas of weaker signal, these hot spots are likely related to imperfect photonic engineering that causes photons generated via radiative recombination to escape the GaAs layer instead of getting trapped and recycled through the layer. These phenomena lend themselves to more analysis beyond the scope of the present work.

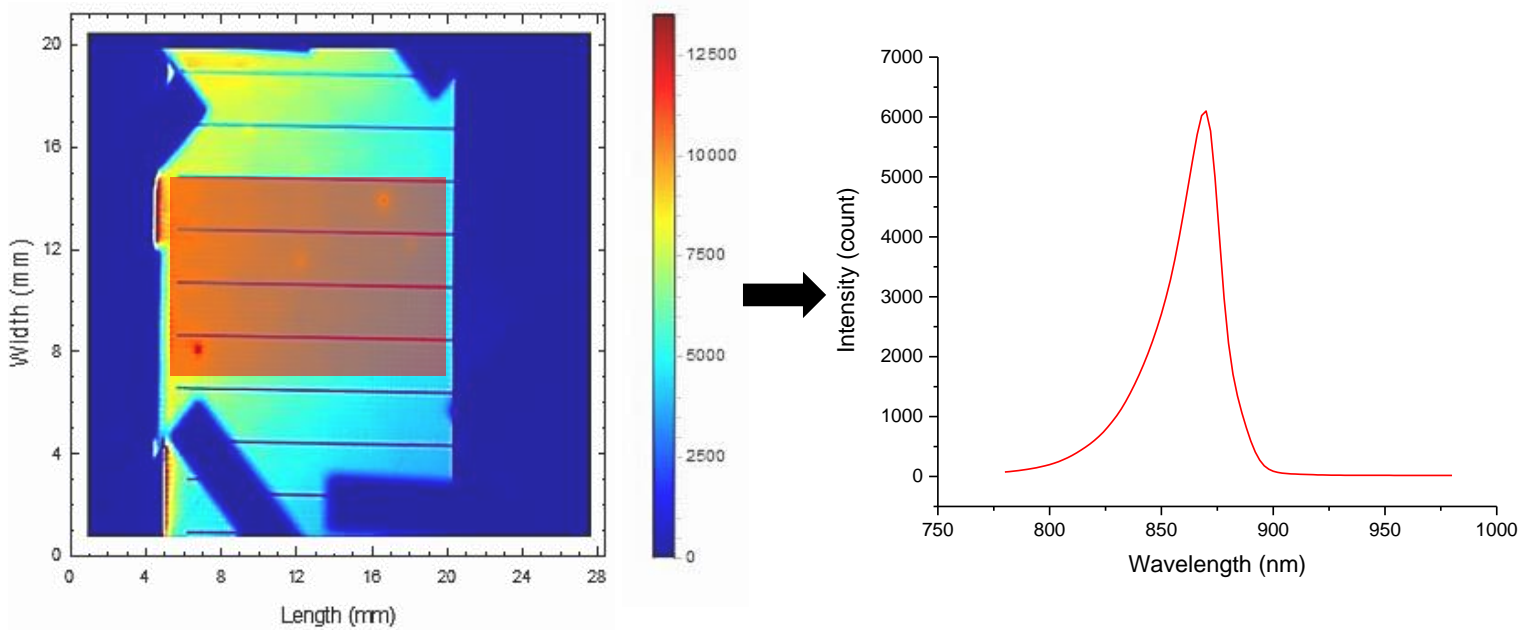


Figure 16: Intensity spectrum using rectangle area

If a sample area is selected on the hyperspectral image, we can plot a spectrum of the intensity in *average* net counts as shown in figure 16. As expected, we see that the peak of the spectrum is located at 870 nm which corresponds to the bandgap of GaAs. Since the area selected is averaged, this spectrum intensity represents the average of all the low and high counts in that region. However, if we were to select each of the hot spots with a tool called a Target, and plot them in comparison to the original spectrum, we would see that the intensity is much higher than the intensity when a

rectangular area is selected. This is shown in figure 17. The particular shape of the spectra such as broadening of the tail regions also give clues to various physical phenomena in a material and the hyperspectral imaging provides for a way to capture all this information in one data cube.

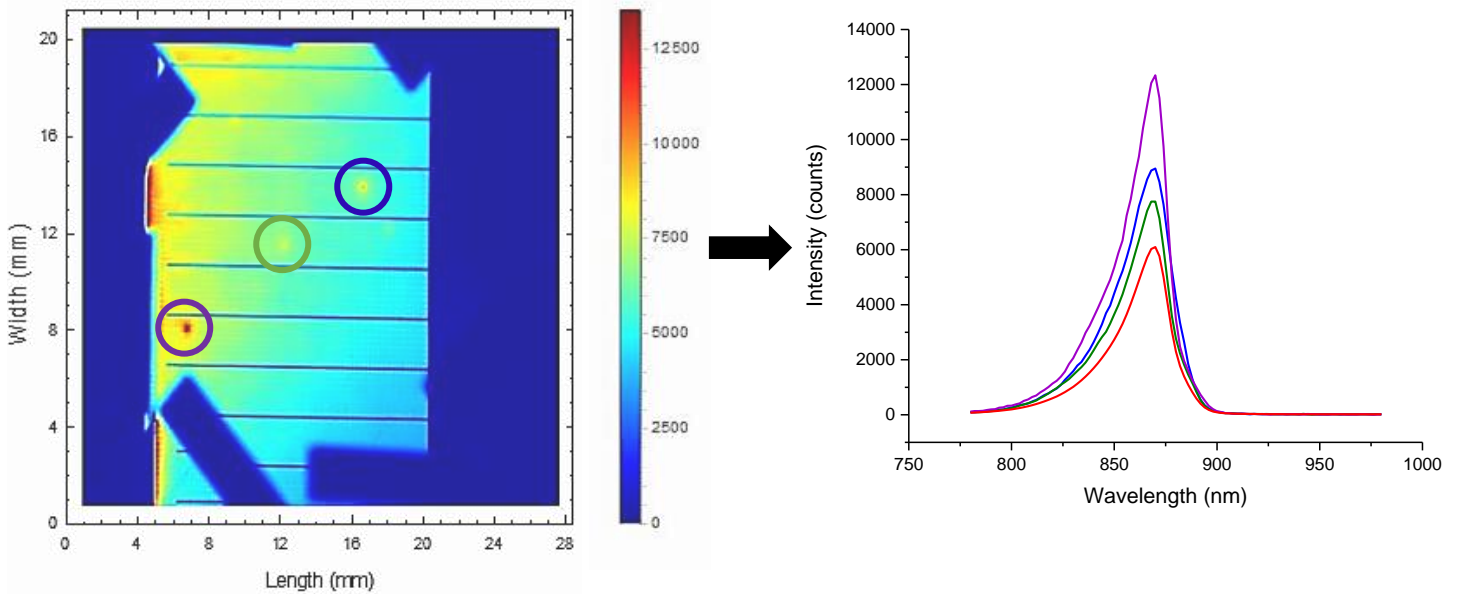


Figure 17: Intensity spectrum of each hot spot in comparison with intensity spectrum using rectangle area

2.4 Calibration of Hyperspectral Cube Data

Looking at the intensity plots from section 2.3, we see that they are counts vs. wavelength. Measuring data in counts may be acceptable when one is only interested in a qualitative image or a relative analysis of various regions of the image. However, we need the absolute scale to be able to use the data for quantitative analysis. Recall from the reciprocity theorem that the EL intensity is given by $\varphi_{em}(E, V) = EQE(E)\varphi_{bb}(E) \exp\left(\frac{qV}{kT}\right)$. Doing the unit analysis as shown below, we can see that

the units of EL intensity should be $\frac{\text{photons}}{\text{m}^2 \cdot \text{s} \cdot \text{eV}}$.

$$\begin{aligned} \varphi_{em}(E, V) &= EQE(E)\varphi_{bb}(E) \exp\left(\frac{qV}{kT}\right) = \textit{unitless} \cdot \frac{\textit{photons} \cdot \textit{eV}^2}{\textit{eV}^3 \cdot \textit{s}^3 \cdot \frac{\textit{m}^2}{\textit{s}^2}} \cdot \textit{unitless} \\ &= \frac{\textit{photons}}{\textit{m}^2 \cdot \textit{s} \cdot \textit{eV}} \end{aligned}$$

Therefore, we must apply a calibration factor to our hyperspectral data (to the net counts) in order to convert intensity in counts to more meaningful units of $\frac{\textit{photons}}{\textit{m}^2 \cdot \textit{s} \cdot \textit{eV}}$. In order to achieve this, we first obtained the spectral irradiance (units: $\frac{\textit{W}}{\textit{m}^2 \cdot \textit{nm}}$) of a quartz-tungsten-halogen (QTH) lamp using a spectroradiometer which gives us the intensity of light over a range of wavelengths. This QTH lamp was coupled into a 2-inch integrating sphere and a 4 mm pinhole aperture was placed at the exit port. The spectroradiometer that we used to measure the irradiance at the plane of the pinhole aperture was calibrated using a NIST traceable lamp to ensure that our spectral irradiance data is accurate. Figure 18 below shows a plot of the spectral irradiance of our QTH light source. Further information on why we decided to use a QTH will be explained later in this section.

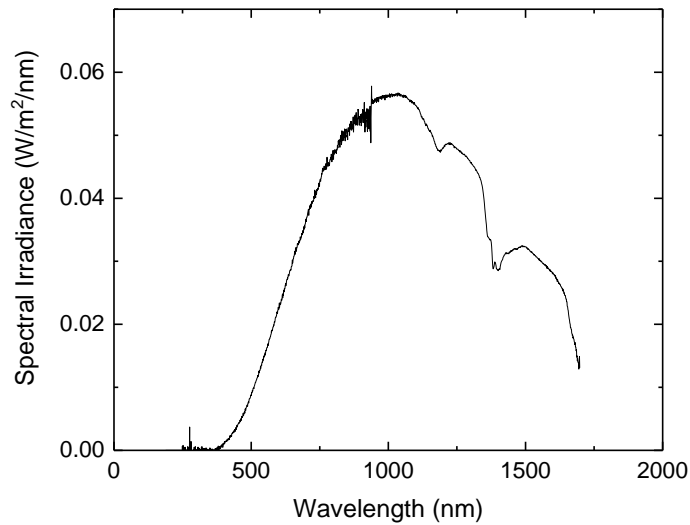


Figure 18: Spectral Irradiance of QTH

We then took hyperspectral imaging data on the QTH-illuminated pinhole aperture so that we obtained plots of intensity in counts vs. wavelength. To obtain the calibration factor (CF), we convert the spectral irradiance to the desired units of $\frac{\text{photons}}{m^2 \cdot s \cdot eV}$ and divide that quantity by the net count for the QTH. The mathematical steps to calculate the CF are detailed below.

We must first convert the spectral irradiance from the spectrometer from units of $\frac{W}{m^2 \cdot nm}$ to $\frac{W}{m^2 \cdot eV}$. Let us denote the spectral irradiance in $\frac{W}{m^2 \cdot nm}$ as $\frac{dE_{rad}}{d\lambda}$ and the spectral irradiance in $\frac{W}{m^2 \cdot eV}$ as $\frac{dE_{rad}}{dE_{ph}}$. E_{ph} is the photon energy in eV .

$$\frac{dE_{rad}}{d\lambda} = \frac{dE_{rad}}{dE_{ph}} \cdot \frac{E_{ph}}{\lambda} \quad (2.4)$$

$$\frac{dE_{rad}}{dE_{ph}} = \frac{dE_{rad}}{d\lambda} \cdot \frac{\lambda}{E_{ph}} \quad (2.5)$$

Note that the λ in equation 2.5 above must be in nm . Now that we have the spectral irradiance in terms of $\frac{W}{m^2 \cdot eV}$, we must convert to photon flux per eV , which we will denote as φ_{cal} , as shown below in order to compare it with our hyperspectral imaging data. Let us denote the photon flux per eV as φ_{cal} . Doing the unit analysis, we see that the λ now has to be in m .

$$\varphi_{cal} = \frac{dE_{rad}}{dE_{ph}} \cdot \frac{\lambda}{hc} \quad (2.6)$$

$$\varphi_{cal} = \frac{W}{m^2 \cdot eV} \cdot \frac{1}{J} = \frac{\text{photons}}{m^2 \cdot s \cdot eV}$$

Finally, we can calculate the calibration factor CF as follows.

$$CF = \frac{\varphi_{cal}}{LCR \text{ of QTH}} \quad (2.7)$$

where LCR is the *light count rate* defined below.

$$\text{light count rate (LCR)} = \frac{\text{light count}}{\text{exposure time}}$$

Recall that in section 2.3, we mentioned that “light” refers to the condition where a voltage is applied across the solar cell and “dark” refers to the condition where there is no applied voltage across the cell. Therefore, “light count” is defined as follows.

$$\text{light count} = \text{total count} - \text{dark count}$$

The count rate we obtain from the hyperspectral imaging data can be multiplied by this CF to get the absolute EL spectrum. Let us denote the absolute EL intensity as φ_{cell} in the desired units.

$$\varphi_{cell} = LCR \text{ of solar cell} * CF \left[\frac{\text{photons}}{m^2 \cdot s \cdot eV} \right] \quad (2.8)$$

In order to obtain the calibration factor, we needed to follow this process of obtaining spectral irradiance data using a spectroradiometer as well as hyperspectral imaging data and then performing the calculations outlined above. Ultimately, we ended up using a QTH illuminated pinhole to perform these tasks but initially, we thought of using LEDs of different wavelengths (i.e. 660 nm, 850 nm, and 940 nm) to obtain calibration factors for different junctions of a multijunction cell. For example, 660 nm corresponds to the wavelength peak of GaInP. Although we did have limited success, however, we soon found out that the very narrow LED emission profiles coupled with very narrow luminescence signals for some materials such as GaAs results in “cross-talk” in the calibration factor, meaning the calibration factor does not end up eliminating the underlying shape of the LED itself. The likely reason for the cause of this is that the hyperspectral imager has a wavelength resolution of 2.5 nm in the

visible range, whereas the spectroradiometer has a resolution of less than 1 nm. Therefore, very narrow peaks present a problem here. In summary, the calibrating light source needs to be a broad-band light source itself and QTH fits that description well. Figure 19 shows the spectral irradiance data for the 850 nm LED that we initially tried to use for the GaAs intensity calibrations and we can see that the peak is very narrow.

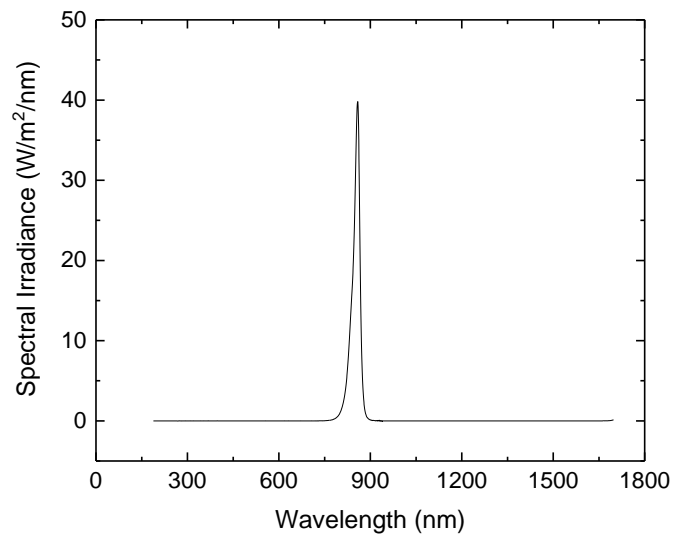


Figure 19: Spectral Irradiance of 850 nm LED

2.4 Hyperspectral Cube Images for a GaAs Solar Cell

Figure 20 below shows an example of the types of images that can be obtained using hyperspectral imaging. The images shown are for a GaAs solar cell at 820 nm, 870 nm which is the wavelength corresponding to the bandgap energy of GaAs and at 890 nm.

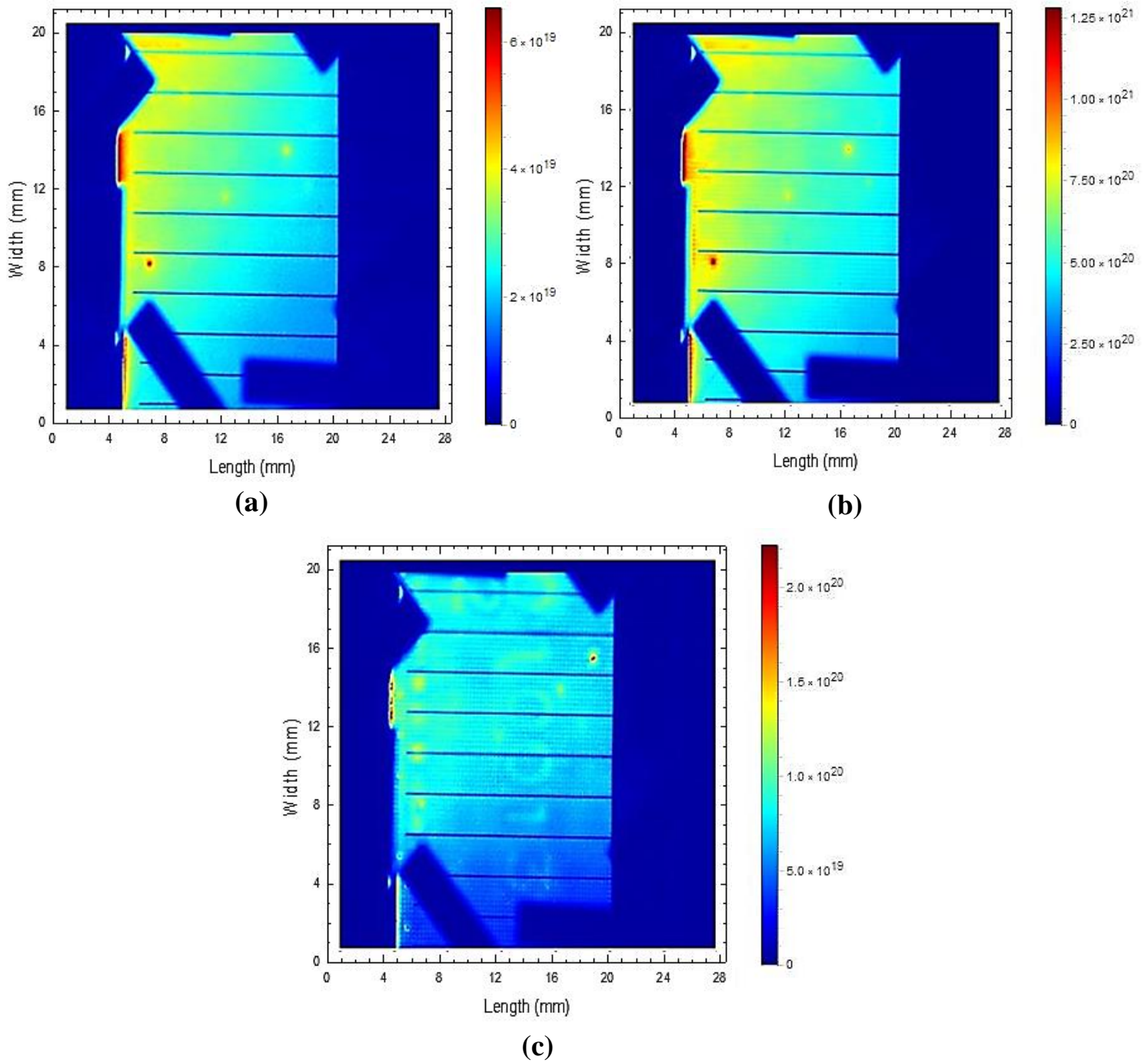


Figure 20: Hyperspectral Imaging data for a GaAs Solar Cell at (a) 820 nm, (b) 870 nm, and (c) 890 nm

From these images, we are able to see many features of the cell such as hot spots as we discussed earlier and the texturing on the top of the cell from the manufacturing

process. As we increase the wavelength to 890 nm, we are also able to see the numbers which are stamped on the back contact of the solar cell by the manufacturers. One question that might arise is why these numbers are visible at 890 nm but not at 820 nm or 870 nm. The absorption coefficient for GaAs decreases with increasing wavelength which means that the chance of photons getting absorbed is much lower at 890 nm as compared to 820 nm or 870 nm [46]. Therefore, the photons have a higher chance of penetrating through the solar cell and reflecting off of the back contact allowing for the stamped numbers to be visible.

The next chapter will focus on discussing the results from the experimental data. It is noted that although hyperspectral imaging allows us to image entire areas of devices, ultimately our quantitative data will be presented by selecting a region of the device close in size to the whole device area and obtaining an average count from that region. This averaged net count data can then be converted to absolute photon flux and used in the context of the reciprocity relationship and compared with global device measurements such as I-V curve measurements. Therefore, the imaging capabilities of the hyperspectral system were not necessarily needed for the analysis that is presented in chapter 3 and were only used to extract an average EL signal from the entire device. Fortunately, the multijunction solar cells that we probed were extremely uniform across entire device areas with minimal interesting features or local variations.

Chapter 3: Characterizing Subcell Losses in Multijunction Solar Cells

3.1 Different Multijunction Solar Cells

We took data on three different triple-junction solar cells labeled as follows: Solar Junction, EMCORE, SPECTROLAB. The Solar Junction cell consisted of GaInP/GaAs/GaInNAs junctions and has an area of 0.988 cm^2 . The EMCORE and SPECTROLAB cells both consisted of GaInP/GaAs/Ge junctions but were made by different manufacturers. The EMCORE cell has an area of 0.818 cm^2 and the SPECTROLAB cell has an area of 2.27 cm^2 . Throughout this chapter, the three junctions of the cells may be referred to by their semiconductor names or by “top junction,” “middle junction” and “bottom junction.” The loss parameters presented in this paper are for the cells working at maximum power point and in order to find the maximum power point, we must have the I-V curves of not only the whole device but each subcell (junction). Of course since these triple junction solar cells each consist of three series-connected cells, we cannot directly measure each junction’s I-V curve. The current-dependent EL measurements that are presented in this chapter provide for a reliable way to compute each junction’s unique I-V curve. The methods to calculate the I-V curves and ultimately the losses will be presented in this chapter.

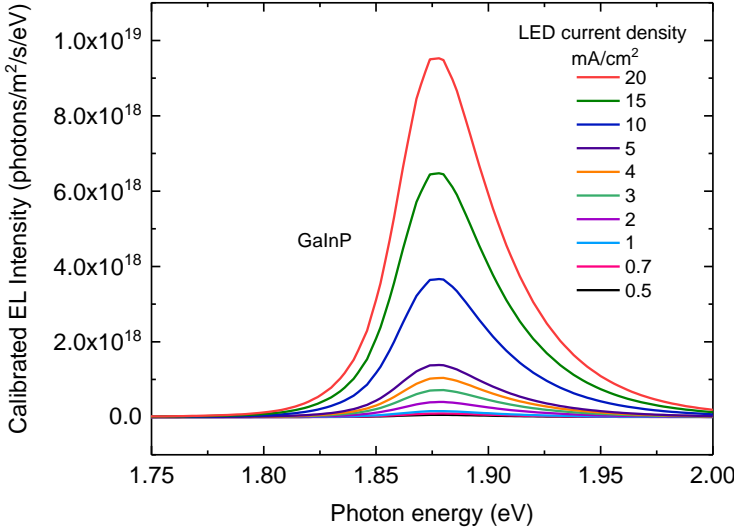
3.2 Calculation of I-V curves from Electroluminescence Data

The objective of this study is to verify a process to characterize each subcell in a multijunction solar cell by taking absolute EL data from each subcell within the multijunction stack. The optical losses, which are used in turn to determine nonradiative losses, are some of the key parameters in such characterization. The loss

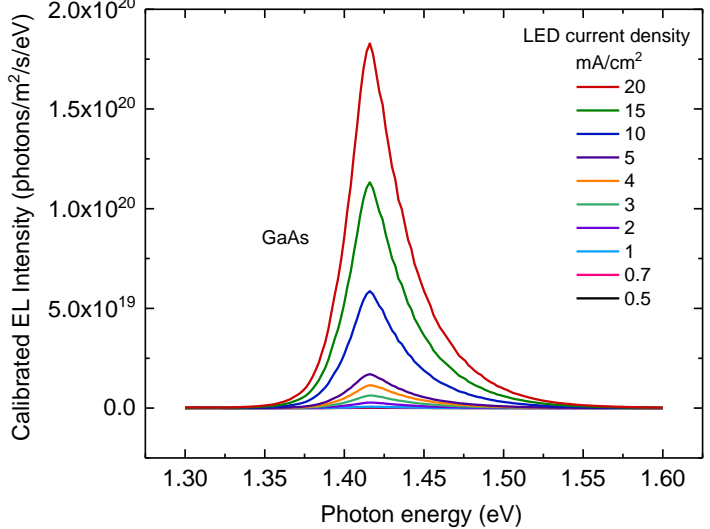
parameters are to be obtained for the solar cell operating at maximum power point because we want to know how much of the incident power is going into losses when the output power is greatest from the solar cell. However, we will not know the maximum power point unless we obtain the I-V curves. We follow the methodology outlined by Chen et. al [47], with the exception that we made some modifications to the carrier balance equations (discussed below) to make them more accurately representative of the carrier balance process. We show that by going through a series of calculations associated with four main figures, we can predict the I-V curves. The four main figures presented for each solar cell are 1) Absolute EL spectra with a series of injection current densities, 2) External EL quantum efficiency y_{ext}^{LED} as a function of injection current density J_{LED} , 3) External luminescence quantum efficiency y_{ext} as functions of solar cell current density J , and 4) I-V curves of the three-junction solar cells. This section will elaborate on the methods used in order to go from our calibrated EL intensity curves to I-V curves and will be organized according to the figures.

3.2.1 Absolute EL spectra with multiple injection current densities

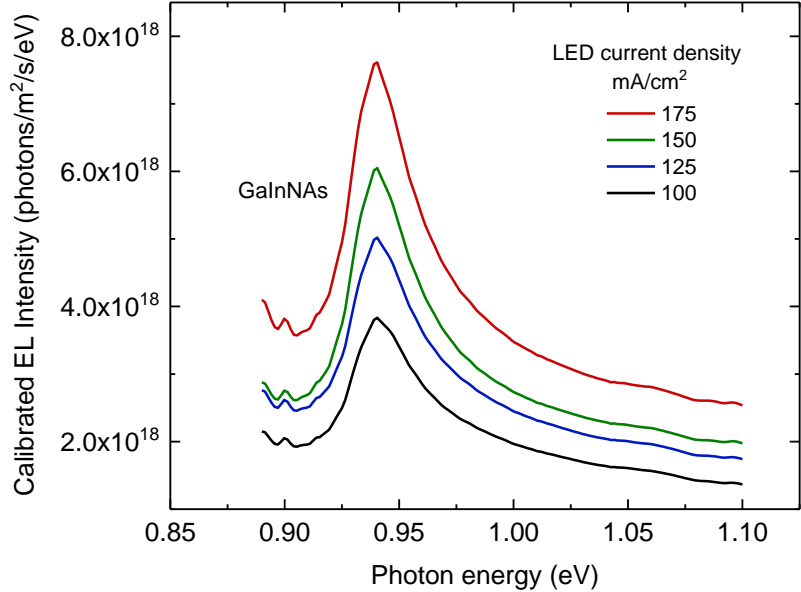
As explained in chapter 2, we must first apply a calibration factor to our raw background-subtracted hyperspectral imaging data in order to arrive at the absolute EL photon flux $R_{ext_{i \rightarrow 0}}(E)$ in units $\frac{photons}{m^2 \cdot s \cdot eV}$. Note that $R_{ext_{i \rightarrow 0}}$ is the same as φ_{cell} in equation 2.8. Figure 21 shows the $R_{ext_{i \rightarrow 0}}$ plots for each junction of the Solar Junction cell.



(a) Top Junction: GaInP



(b) Middle Junction: GaAs



(c) Bottom Junction: GaInNAs

Figure 21: Absolute EL Photon Flux $R_{ext_{i \rightarrow 0}}$ for each junction of the Solar Junction cell

To calculate the absolute values for EL intensity, the EL photon flux is divided by the current density in terms of the number of electrons. This is shown in equation 3.1 below.

$$\frac{R_{ext_{i \rightarrow 0}}}{J_{LED}} = \frac{\frac{\text{photons}}{m^2 \cdot s \cdot eV}}{\frac{C}{s \cdot m^2}} = \frac{\frac{\text{photons}}{m^2 \cdot s \cdot eV}}{\frac{\text{electrons}}{s \cdot m^2}} = \frac{\text{photons}}{\text{electrons} \cdot eV} \quad (3.1)$$

Plotting $\frac{R_{ext_{i \rightarrow 0}}}{J_{LED}}$ as a function of energy eV , the absolute EL spectrum is obtained and

we repeat this process for the other injection current densities. It is noted that we obtain the J_{LED} by taking the sourced current, I_{LED} and dividing it by the nominal device area.

Figure 22 shows the absolute EL spectra for the three solar cells. In general, our EL emission rates for the EMCORE and SPECTRLAB cells, which consisted of GaInP/GaAs/Ge junctions, were lower in magnitude than those presented in the Chen et. al paper compared at similar current densities. This may be due to variations in cell manufacturing. We can also notice that in all three of the cells, the middle junction GaAs for all three cells has a higher EL peak compared to the top junction GaInP. This suggests a higher amount of radiative recombination in GaAs as compared to GaInP for the same current density. Furthermore, the SPECTROLAB EL intensities are in general lower even though higher current densities were applied. For the GaInNAs junction on the Solar Junction cell, we needed to go to relatively high current densities in order to obtain a noticeable signal in our hyperspectral imager. Even at such high current densities, the EL intensities are very small as seen in figure 22a.

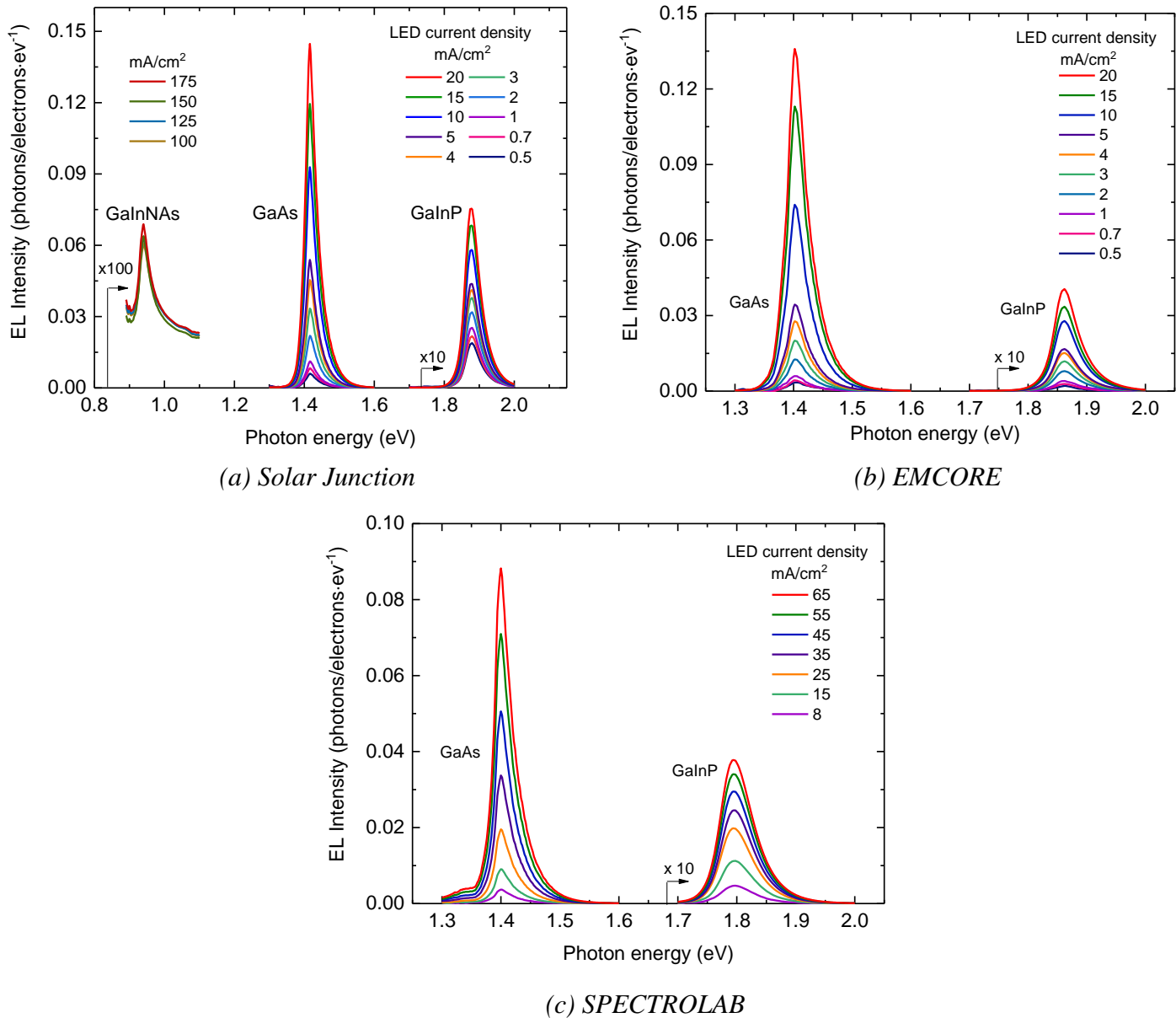


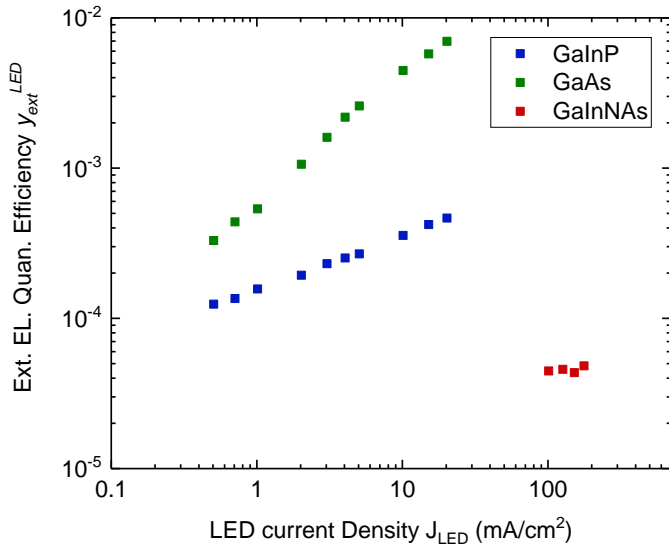
Figure 22: Absolute EL Spectra for each cell

3.2.2 External EL quantum yield y_{ext}^{LED} vs. J_{LED}

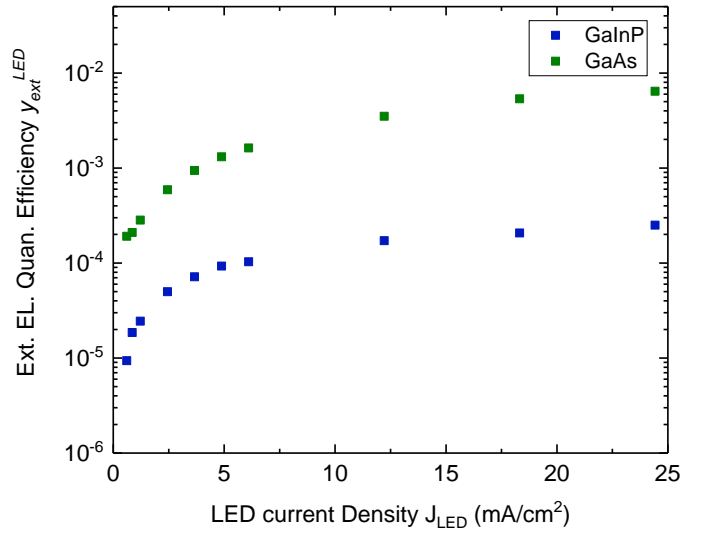
External EL quantum yield gives the ratio of the number of photons emitted out from the junction over the electrons injected in. In order to obtain a plot of this EL quantum efficiency as a function of the injection current density, the absolute EL

spectra which are in units $\frac{\text{photons}}{\text{electrons}\cdot\text{eV}}$ as a function of eV can simply be integrated to obtain the quantum yield over all emission energies. This process gives the y_{ext}^{LED} shown in Fig. 23.

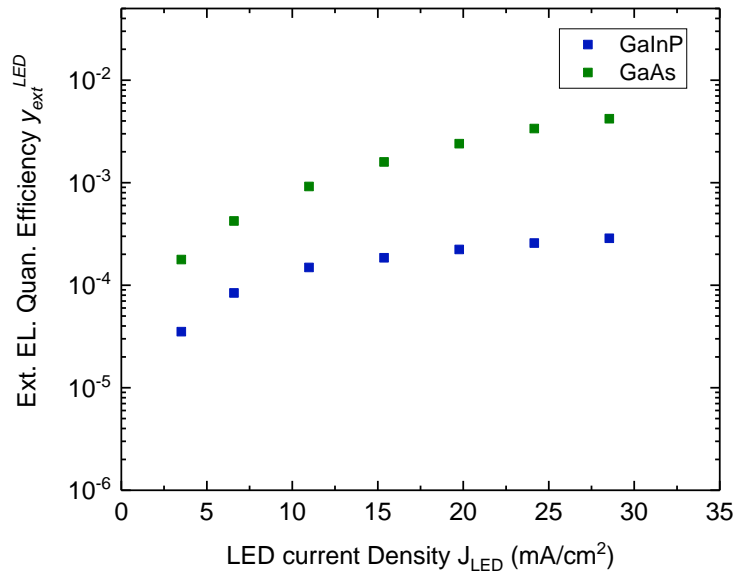
The plot for the Solar Junction cell is shown on a log-log scale due to the high current densities of the GaInNAs junction. We can see that the higher the magnitude of the EL peak, the higher the magnitude of the y_{ext}^{LED} . The SPECTROLAB cell had lower magnitudes for the EL peak and therefore the y_{ext}^{LED} s for all of the junctions are lower in magnitude. In general, we notice that the external EL quantum efficiency increases with increasing injection current density although this increase begins to plateau for the EMCORE and SPECTROLAB cells. The higher quantum yield at higher current densities is the result of increased radiative recombination in these materials because defect-mediated non-radiative recombination phenomena tend to slightly saturate at higher injection levels.



(a) Solar Junction



(b) EMCORE



(c) SPECTROLAB

Figure 23: y_{ext}^{LED} plots

3.2.3 External luminescence quantum yield y_{ext}

The external luminescence quantum yield or efficiency y_{ext} is the same as the external EL quantum efficiency y_{ext}^{LED} when the number of carriers in the device

under the solar cell operation is the same as when measured in the injection (LED) mode. The y_{ext} is expressed as a function of the solar current density J whereas the y_{ext}^{LED} is expressed as a function of injection current density J_{LED} . The y_{ext} can be derived based on carrier balance equations presented below.

Carrier Balance Equations

Since our 3-junction solar cells are series-connected internally within the stacked layers and in order of decreasing band gap (i.e. $E_{g1} > E_{g2} > E_{g3}$), we can use the following carrier balance equations to describe the optoelectronic processes that occur due to irradiating the solar cell with sunlight [47].

$$R_{Sun_1} + \frac{J}{q} = R_{ext_{1 \rightarrow 0}} + R_{ext_{1 \rightarrow 2}} + R_{nr_1} \equiv \left(\frac{1}{y_{ext_1}} \right) R_{ext_{1 \rightarrow 0}} \quad (3.2)$$

$$R_{Sun_2} + \frac{J}{q} + R_{ext_{1 \rightarrow 2}} = R_{ext_{2 \rightarrow 0}} + R_{ext_{2 \rightarrow 3}} + R_{nr_2} \equiv \left(\frac{1}{y_{ext_2}} \right) R_{ext_{2 \rightarrow 0}} \quad (3.3)$$

$$R_{Sun_3} + \frac{J}{q} + R_{ext_{2 \rightarrow 3}} = R_{ext_{3 \rightarrow 0}} + R_{ext_{3 \rightarrow S}} + R_{nr_3} \equiv \left(\frac{1}{y_{ext_3}} \right) R_{ext_{3 \rightarrow 0}} \quad (3.4)$$

In the above equations, $R_{Sun_i} = \int EQE_i(E) S_{AM0}(E) dE$ is the absorption rate of the sunlight where the subscript i refers to each subcell ($i = 1, 2$ and 3). EQE_i is the external quantum efficiency of each subcell and S_{AM0} is the AM0 photon flux per energy in units $\frac{photons}{m^2 \cdot s \cdot eV}$. The method for conducting EQE measurements can be found in reference [48]. J is the solar cell current density where + is for forward bias injection current and - is for photogenerated current. $R_{ext_{i \rightarrow 0}}$ is the external radiative emission rate which means the number of photons (per unit area per second per eV) that are produced as a result of radiative recombination. The subscript 0 refers to air and the direction of the arrows indicate the direction of the emissions, i.e., from

junction to air where they are detected by camera. The values of $R_{ext_{i \rightarrow 0}}$ were experimentally obtained using electroluminescence measurements and this will be further explained in future sections. $R_{ext_{i \rightarrow i+1}}$ is the luminescence coupling (LC) rate which is the radiative emission from junction i which is emitted into junction $i + 1$. The LC effect is basically the result of the same radiative recombination process that gives $R_{ext_{i \rightarrow 0}}$, with the difference that the emitted photons are emitted down towards the lower band gap junction below. Notice that this luminescence typically occurs at the edge of the band gap and therefore the emitted photons have similar energies as the size of the band gap. When the reflectivity of the interfaces is very close to zero at the upper and lower regions of the i^{th} subcell and $n_i < n_{i+1}$, where n_i is the index of refraction of junction i , the expression for luminescence coupling simplifies to $R_{ext_{i \rightarrow i+1}} = n_i^2 R_{ext_{i \rightarrow 0}}$. The nonradiative recombination rate, which is a major recombination mechanism in these devices is represented by R_{nr_i} , and $R_{ext_{3 \rightarrow S}}$ shows the radiative emission from junction 3 to the substrate and is set to 0 for the devices presented in this paper because it is insignificant compared to other terms. y_{ext_i} is the luminescence quantum yield which represents the number of electrons that are converted to photons when the device is operated in solar cell mode.

The first equalities show a carrier balance between the number of carriers generated and the number of carriers that recombine, both radiative and nonradiative. This carrier balance is equivalent to dividing the radiative emission $R_{ext_{i \rightarrow 0}}$ by the luminescence yield y_{ext_i} as shown in the second equalities. We can now see that the

y_{ext_i} and the external radiative emission rate $R_{ext_{i \rightarrow 0}}$ can be expressed as a function of the incident carriers.

$$y_{ext_1}[J] \left(R_{sun_1} + \frac{J}{q} \right) = R_{ext_{1 \rightarrow 0}}[J] \quad (3.5)$$

$$y_{ext_2}[J] \left(R_{sun_2} + \frac{J}{q} + R_{ext_{1 \rightarrow 2}} \right) = R_{ext_{2 \rightarrow 0}}[J] \quad (3.6)$$

$$y_{ext_3}[J] \left(R_{sun_3} + \frac{J}{q} + R_{ext_{2 \rightarrow 3}} \right) = R_{ext_{3 \rightarrow 0}}[J] \quad (3.7)$$

where the brackets $[J]$ indicate that y_{ext_i} is a function of J , the current density in the solar cell mode operation. We can also express y_{ext}^{LED} and $R_{ext_{i \rightarrow 0}}$ as a function of the incident carriers in LED mode as shown in the following equations. The absolute EL spectra in section 3.2.1 can also be calculated using these equations.

$$y_{ext_1}^{LED}[J_{LED}] \left(\frac{J_{LED}}{q} \right) = R_{ext_{1 \rightarrow 0}}[J_{LED}] \quad (3.8)$$

$$y_{ext_2}^{LED}[J_{LED}] \left(\frac{J_{LED}}{q} + R_{ext_{LED\ 1 \rightarrow 2}} \right) = R_{ext_{2 \rightarrow 0}}[J_{LED}] \quad (3.9)$$

$$y_{ext_3}^{LED}[J_{LED}] \left(\frac{J_{LED}}{q} + R_{ext_{LED\ 2 \rightarrow 3}} \right) = R_{ext_{3 \rightarrow 0}}[J_{LED}] \quad (3.10)$$

Obtaining J as a function of J_{LED}

Since we do not conduct experiments in solar cell operation, we are not able to measure the luminescence quantum yield y_{ext_i} . We know that the y_{ext_i} should equal the external EL quantum efficiency $y_{ext_i}^{LED}$ given that the number of carriers in the device are the same. This assumption is taken for simplicity [49]. As a result, we must solve for the solar cell current density J in terms of J_{LED} , so we can perform this

equivalency. For junction 1, we can solve for J by equating the two current densities as shown below.

$$y_{ext_1} \left(R_{sun_1} + \frac{J}{q} \right) = y_{ext_1}^{LED} \left(\frac{J_{LED}}{q} \right) \quad (3.11)$$

$$qR_{sun_1} + J = J_{LED} \rightarrow J = J_{LED} - qR_{sun_1} \quad (3.12)$$

For junction 2 and junction 3, we have a luminescent coupling term present with the $R_{ext_{i \rightarrow i+1}}$ as we can see in the solar cell current densities. We included the luminescent coupling term for the cell in LED operation as well, which is denoted as $R_{ext_{LED_{i \rightarrow i+1}}}$. As a result, we have two implicit functions: one for J and one for J_{LED} .

For junction 2, we have the following equations.

$$y_{ext_2} \left(R_{sun_2} + \frac{J}{q} + R_{ext_{1 \rightarrow 2}} \right) = y_{ext_2}^{LED} \left(\frac{J_{LED}}{q} + R_{ext_{LED_{1 \rightarrow 2}}} \right) \quad (3.13)$$

$$qR_{sun_2} + J + qR_{ext_{1 \rightarrow 2}} = J_{LED} + qR_{ext_{LED_{1 \rightarrow 2}}} \quad (3.14)$$

Following the definition for luminescence coupling, we can expand $R_{ext_{1 \rightarrow 2}}$ and $R_{ext_{LED_{1 \rightarrow 2}}}$ as follows.

$R_{ext_{1 \rightarrow 2}} = n_1^2 R_{ext_{1 \rightarrow 0}}[J]$ where

$$R_{ext_{1 \rightarrow 0}}[J] = y_{ext_1} \left(R_{sun_1} + \frac{J}{q} \right)$$

$R_{ext_{LED_{1 \rightarrow 2}}} = qn_1^2 R_{ext_{LED_{1 \rightarrow 0}}}[J_{LED}]$ where

$$R_{ext_{LED_{1 \rightarrow 0}}}[J_{LED}] = y_{ext_1}^{LED} \left(\frac{J_{LED}}{q} \right)$$

For junction 3, we follow the same steps by setting equal y_{ext_3} and $y_{ext_3}^{LED}$.

$$y_{ext_3} \left(R_{sun_3} + \frac{J}{q} + R_{ext_{2 \rightarrow 3}} \right) = y_{ext_3}^{LED} \left(\frac{J_{LED}}{q} + R_{ext_{LED_{2 \rightarrow 3}}} \right) \quad (3.15)$$

$$qR_{sun_3} + J + qR_{ext_{2 \rightarrow 3}} = J_{LED} + qR_{ext_{LED_{2 \rightarrow 3}}} \quad (3.16)$$

Following the definition for luminescence coupling once again, we can expand

$R_{ext_{2 \rightarrow 3}}$ and $R_{ext_{LED_{2 \rightarrow 3}}}$ as follows.

$R_{ext_{2 \rightarrow 3}} = n_2^2 R_{ext_{2 \rightarrow 0}}[J]$ where

$$R_{ext_{2 \rightarrow 0}}[J] = y_{ext_2} \left(R_{sun_2} + \frac{J}{q} + R_{ext_{1 \rightarrow 2}} \right) * \left(R_{sun_2} + \frac{J}{q} + R_{ext_{1 \rightarrow 2}} \right)$$

$R_{ext_{LED_{2 \rightarrow 3}}} = n_2^2 R_{ext_{LED_{2 \rightarrow 0}}}[J_{LED}]$ where

$$R_{ext_{LED_{2 \rightarrow 0}}}[J_{LED}] = y_{ext_2}^{LED} (J_{LED} + qR_{ext_{LED_{1 \rightarrow 2}}}) * (J_{LED} + qR_{ext_{LED_{1 \rightarrow 2}}})$$

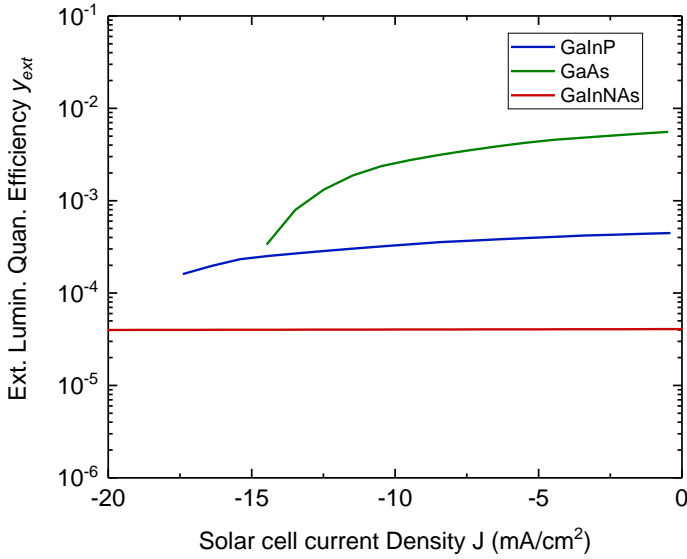
As shown in equations 3.14 and 3.16, we have implicit functions for J and J_{LED} on the left and right-hand sides respectively. After solving these implicit functions, we can find the corresponding solar cell current densities J for a given set of J_{LED} values. We know the y_{ext} values and we now know the solar cell current densities J so we can plot the external luminescence quantum yield as a function of solar cell current density.

The R_{sun} values used for the individual junctions for the three solar cells are presented in Table 3.1 below.

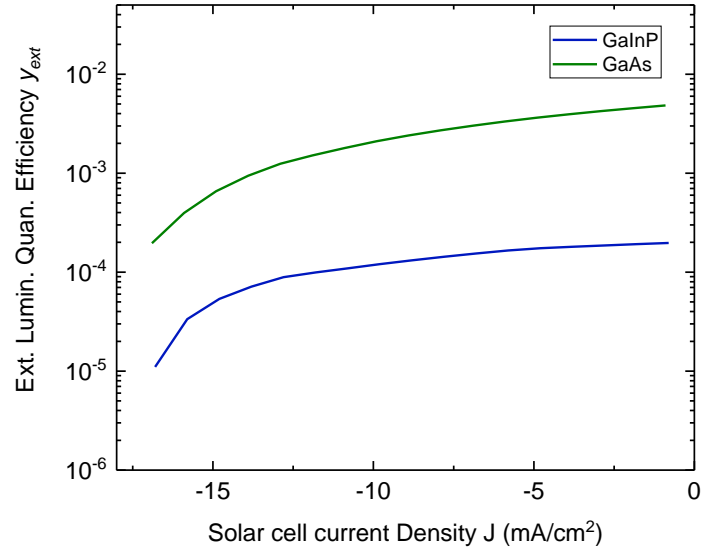
Table 3.1: R_{sun} values for three solar cells under AM 0 spectrum

| $R_{sun_i} (mA/cm^2)$ | <i>Solar Junction</i> | <i>EMCORE</i> | <i>SPECTROLAB</i> |
|-----------------------|-----------------------|---------------|-------------------|
| R_{sun_1} | 18.5103 | 17.4541 | 17.1029 |
| R_{sun_2} | 14.9975 | 17.5734 | 17.2659 |
| R_{sun_3} | 17.5107 | 27.8915 | 30.3002 |

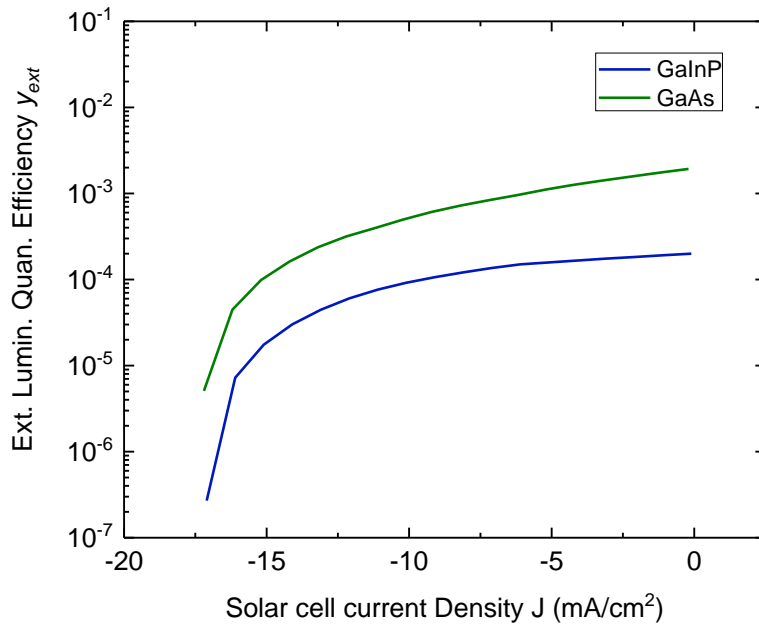
Figures 24 a-c show the plots for y_{ext} for the three solar cells. Note that the y_{ext} is maximum when the solar cell current density is zero, i.e., when each junction is forced to operate near its V_{oc} . It is from these plots that we will be able to calculate



(a) Solar Junction



(b) EMCORE



(c) SPECTROLAB

Figure 24: y_{ext} plots

each subcells's I-V curves. We will see later in this chapter that the y_{ext} plots have an effect on the magnitude of the V_{oc} values.

3.2.4 I-V curves of three junction solar cells

Using the information in the plots of y_{ext} vs. J , we can express the $R_{ext_{i \rightarrow 0}}$ in terms of J and predict the I-V curves according to the reciprocity theorem as detailed below.

Reciprocity Theorem and Prediction of I-V Characteristics

As mentioned in chapter 1, electroluminescence is the reciprocal process to the conventional operation of a solar cell in which light energy is converted to electric energy. The reciprocity theorem allows us to relate the electroluminescence emission rate to the external quantum efficiency and voltage across a particular junction of the solar cell. The electroluminescence emission rate is given by equation 1.20 in chapter 1 and is the quantity $R_{ext_{i \rightarrow 0}}$ that we have been discussing above, restated in equation 3.17 below with a series resistance R_s included to account for any resistance in the contacts and wires. By fitting this equation to EL data taken on each junction's isotype cell, we determined the series resistance to be approximately $R_s \approx 0.315 \Omega$.

$$R_{ext_{i \rightarrow 0}}(E, V) = EQE(E)\phi_{bb}(E) \exp\left(\frac{q(V - IR_s)}{kT}\right) \quad (3.17)$$

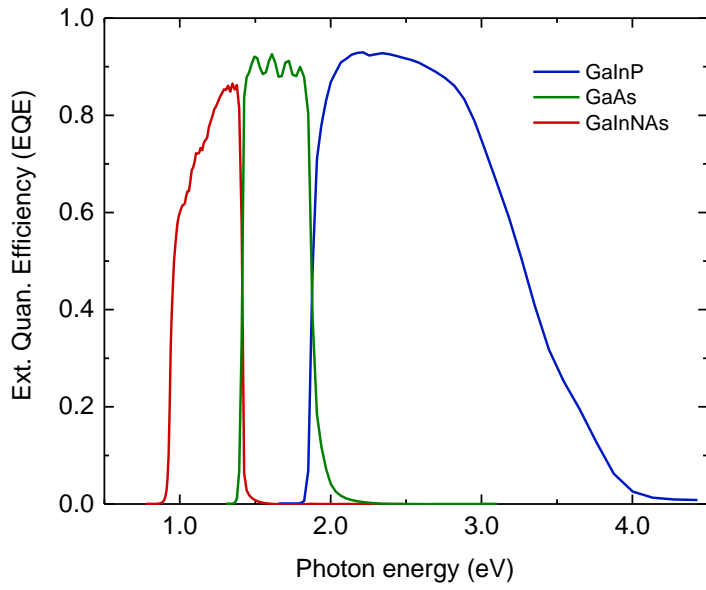
To calculate the I-V curves, we solve for the voltage as a function of J in 3.17. Using the plots of y_{ext} from section 3.2.3, we can calculate the external radiative emission rate $R_{ext_{i \rightarrow 0}}(J)$ as a function of J by using equations 3.5-3.7. Equation 3.18 shows the final expression for the voltage $V_i(J)$ where the subscript i denotes each junction in the solar cell and A is the area of the solar cell.

$$V_i(J) = \frac{kT}{q} \ln \frac{R_{ext_{i \rightarrow 0}}(J)}{\langle EQE_i \rangle_{EL} \int_{E_{g_i}}^{\infty} \varphi_{bb}(E) dE} + (J * A) R_S \quad (3.18)$$

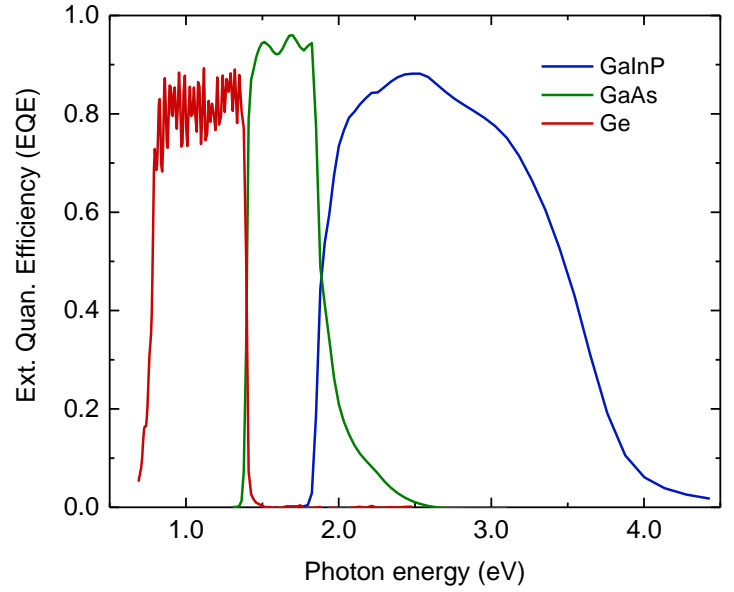
$\langle EQE_i \rangle_{EL}$ is an averaged EQE for each junction calculated by the following equation.

$$\langle EQE_i \rangle_{EL} = \frac{\int EQE_i(E) R_{ext_{i \rightarrow 0}}(E) dE}{\int R_{ext_{i \rightarrow 0}}(E) dE} \quad (3.19)$$

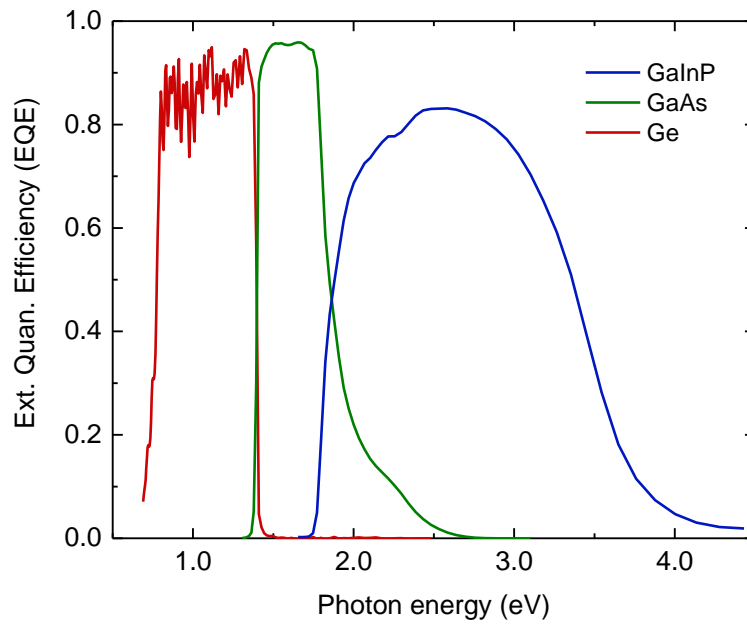
In the absence of trap states, the band gap is the minimum energy required for an electron to be excited to the conduction band of a semiconductor and subsequently generate a current. The EQE gives the ratio of the number of electrons collected from the cell over the number of incident photons and is usually presented over a range of energies. For the calculation of the band gap energies, we followed a standard method where the maximum of $\frac{dEQE_i}{dE}$ gives the E_{g_i} [50]. The EQE distributions for each of the cells are shown in the Figure 25 below. The band gap values used in this paper are shown in table 3.2 below.



(a) Solar Junction



(b) EMCORE



(c) SPECTROLAB

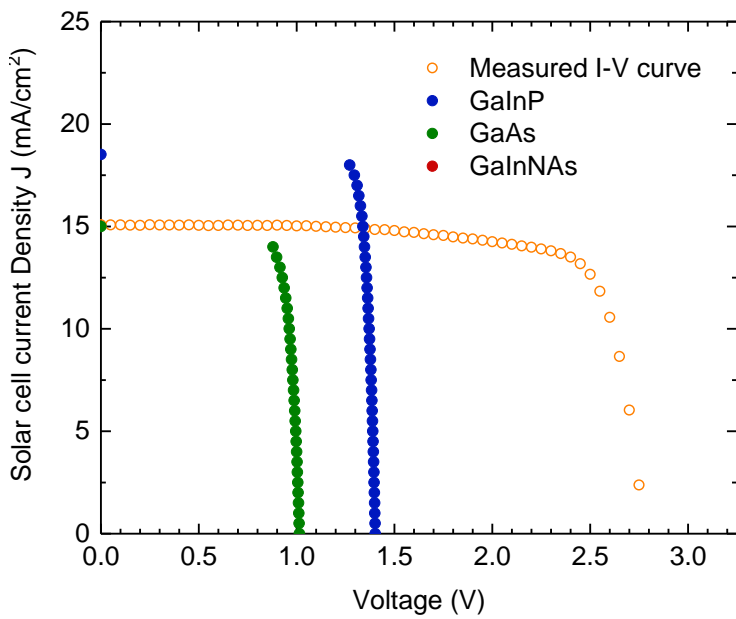
Figure 25: EQE plots

Table 3.2: Band gap energies for each junction for each of the solar cells

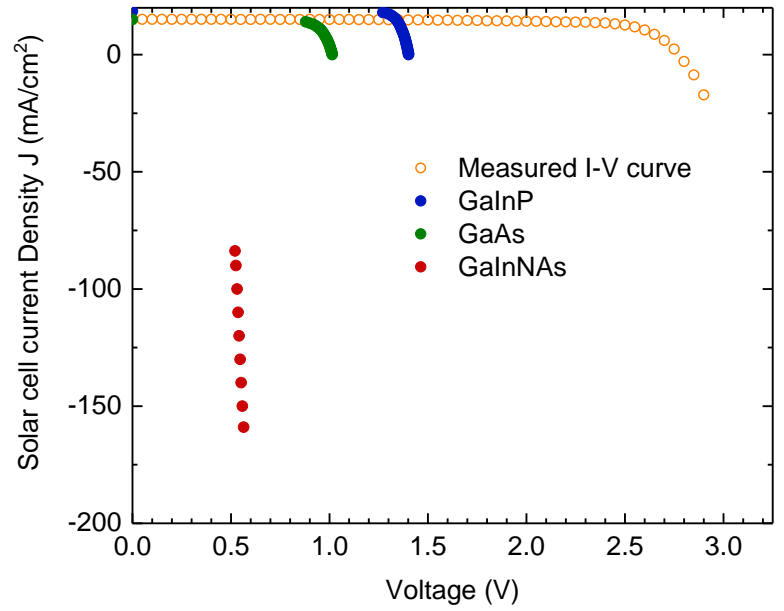
| Bandgaps E_{g_i} (eV) | <i>Solar Junction</i> | <i>EMCORE</i> | <i>SPECTROLAB</i> |
|----------------------------|-----------------------|---------------|-------------------|
| E_{g_1} | 1.87058 | 1.86246 | 1.79821 |
| E_{g_2} | 1.41541 | 1.39975 | 1.40018 |
| E_{g_3} | 0.934377 | *0.69 | *0.69 |

*Due to limitations in our EQE system, we were not able to properly measure the bottom junction for the EMCORE and SPECTROLAB cell. As a result, these band gap energies were taken from the supplementary information of the Chen paper [47]. Figure 26 shows the calculated I-V curves for all three cells. We can see that the y_{ext} plots in figure 24 affect the V_{oc} values in these I-V curves in that the higher the y_{ext} value, the higher the V_{oc} value. For the Solar Junction cell's bottom junction I-V curve data, the current densities are in the negative range and high in magnitude because of high current densities when we were taking EL data. It is also important to notice that although the EMCORE and SPECTROLAB cells consisted of the same type of material, the V_{oc} values for the GaInP and GaAs junction are slightly different. This difference in V_{oc} values arises from the difference in y_{ext} values. As mentioned in equation 1.27 in chapter 1, the V_{oc} includes a loss contribution due to nonradiative recombination equal to $-\frac{kT}{q}\ln(y_{ext})$. For a given junction, the difference in the V_{oc} values for the two different cells is equal to the difference in these loss terms as shown below in equation 3.20.

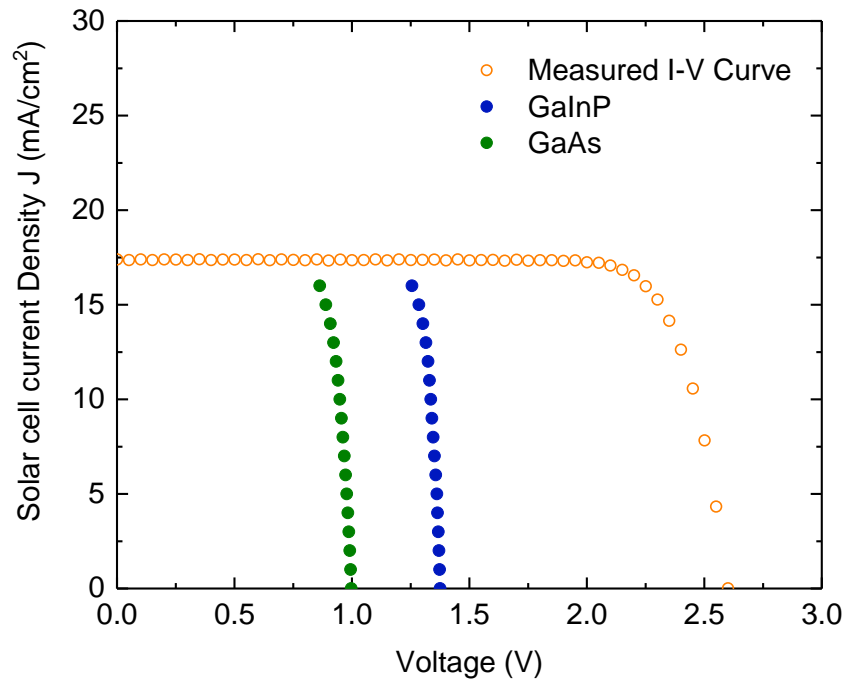
$$\left(-\frac{kT}{q}\ln(y_{ext_{SPECTROLAB}})\right) - \left(-\frac{kT}{q}\ln(y_{ext_{EMCORE}})\right) \quad (3.20)$$



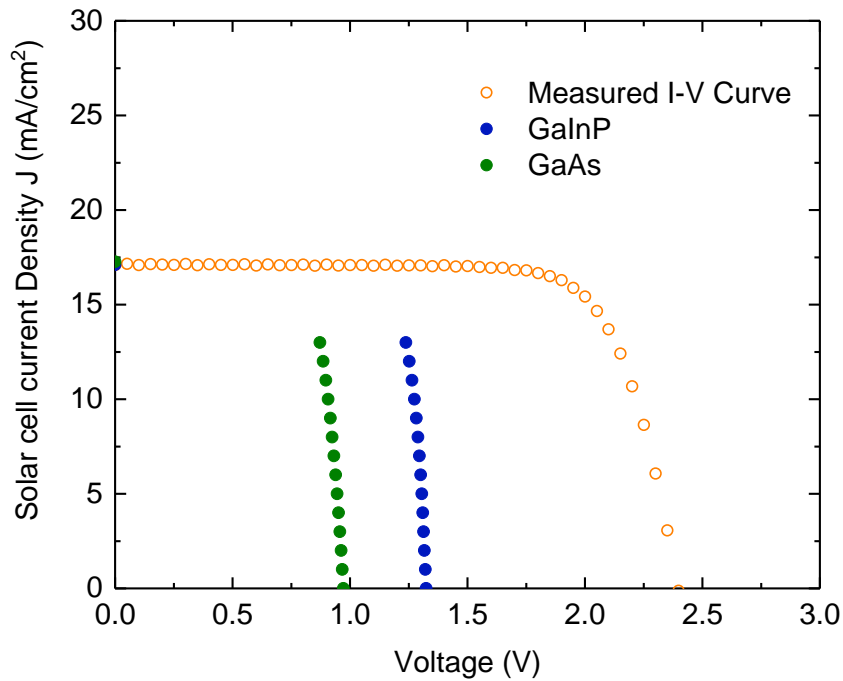
(a) Solar Junction positive J region



(b) Solar Junction negative J region



(c) EMCORE



(d) SPECTROLAB

Figure 26: Calculated I-V Curves

As we can see in figure 26, we were only able to calculate part of the I-V curves. Calculating more complete I-V curves would have required us to take data at lower current densities. We could not take data at lower current densities as we did not have a strong EL signal. We need to know the maximum power point as well as the full shape of the I-V curves in order to calculate the losses so we proceeded to model each junction of our cells with the double diode model.

3.3 Double Diode Model

The double diode model is an equivalent circuit model for a solar cell with two diodes, series resistance and shunt resistance where the diodes represent the diffusion and recombination processes in a solar cell [51]. Figure 27 below shows a schematic of the double diode model equivalent circuit where I_{PH} is the photogenerated current.

We used the double diode model to model the I-V curves for each junction in our solar cells so that we could obtain more complete I-V curves. There is a single diode model which includes only one diode representing the diffusion processes but the double diode model is more accurate for the I-V curve because it takes into account the recombination processes as well [51].

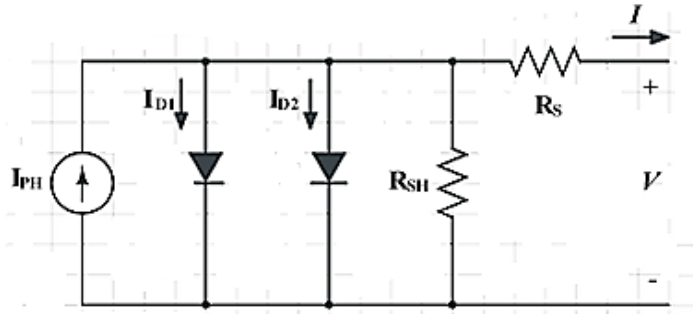


Figure 27: Equivalent circuit schematic of double diode

The expressions for the current density J as a function of voltage V for each junction can be written in both the forward bias direction and the reverse bias direction [48].

$$\begin{aligned}
 J_i(V) = & -J_{i_{ph}} + J_{i_{01}} \left(\exp \left(\frac{e(V - R_{i_s} A J_i(V))}{kT} \right) - 1 \right) \\
 & + J_{i_{02}} \left(\exp \left(\frac{e(V - R_{i_s} A J_i(V))}{n_i kT} \right) - 1 \right) \\
 & + \frac{V - R_{i_s} A J_i(V)}{R_{i_{sh}} A} \quad (\text{forward bias direction}) \quad (3.21)
 \end{aligned}$$

$$\begin{aligned}
J_i(V) = & \left(-J_{i_{ph}} + J_{i_{01}} \left(\exp \left(\frac{e(V - R_{i_s} A J_i(V))}{kT} \right) - 1 \right) \right. \\
& + J_{i_{02}} \left(\exp \left(\frac{e(V - R_{i_s} A J_i(V))}{n_i kT} \right) - 1 \right) + \frac{V - R_{i_s} A J_i(V)}{R_{i_{sh}} A} \\
& \times \frac{1}{1 - \left(\frac{V}{V_{i_{bd}}} \right)^{n_{i_m}}} \text{ (reverse bias direction)} \quad (3.22)
\end{aligned}$$

In the above equations, $J_{i_{ph}}$ is the photogenerated current density of the i^{th} junction, $J_{i_{01}}$ is the saturation current density, $J_{i_{02}}$ is the saturation current density for the depletion region, A is the device area, R_{i_s} is the series resistance, $R_{i_{sh}}$ is the shunt resistance, n_i is the ideality factor, n_{i_m} is the Miller index and $V_{i_{bd}}$ is the breakdown voltage. The expression for the reverse bias direction is multiplied by a factor that accounts for the cell's avalanche breakdown in reverse bias [48].

In order to use the double diode model to obtain more complete I-V curves, we varied each of the parameters $J_{i_{01}}$, $J_{i_{02}}$, R_{i_s} , and $R_{i_{sh}}$ and determined which parameters created a model that best fit the calculated I-V curves from figure 26. The Miller index n_{i_m} and the breakdown voltage $V_{i_{bd}}$ were kept at similar values as reported in literature [48]. Figure 28 below shows the I-V curves using the double diode model. For a given solar cell, we used the best fit for each junction to compute a composite I-V curve. After comparing this composite I-V curve with the I-V curve obtained experimentally, we noticed a discrepancy between the two curves. In order to find an explanation for this discrepancy, we manipulated the parameters of the double diode

model again until the calculated composite I-V curve matched the measured I-V curve. These parameters are summarized in Tables 3.3, 3.4 and 3.5 below.

Table 3.3: Parameters for Solar Junction cell

| Junction | R_s [Ω] | R_{sh} [Ω] | J_{ph} [A/m^2] | J_{01} [A/m^2] | J_{02} [A/m^2] | n | n_m | V_{bd} |
|----------|--------------------|-----------------------|----------------------|----------------------|----------------------|-----|-------|----------|
| GaInP | 0.5 | 5000 | 185.103 | 5×10^{-22} | 1×10^{-6} | 3.3 | 3 | -10 |
| GaAs | 0.5 | 5000 | 149.975 | 9×10^{-16} | 3×10^{-5} | 2.8 | 3 | -10 |
| GaInNAs | 0.5 | 45 | 175.107 | 3×10^{-6} | 8×10^{-2} | 2 | 3 | -10 |

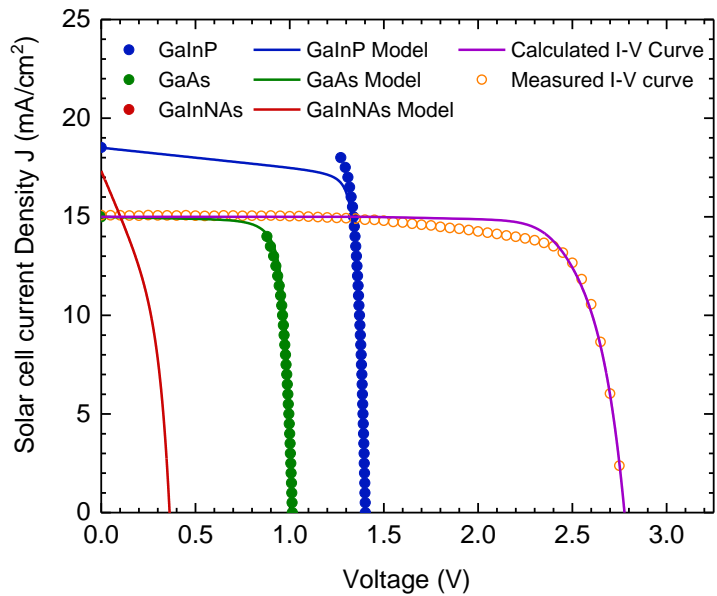
Table 3.4: Parameters for EMCORE cell

| Junction | R_s [Ω] | R_{sh} [Ω] | J_{ph} [A/m^2] | J_{01} [A/m^2] | J_{02} [A/m^2] | n | n_m | V_{bd} |
|----------|--------------------|-----------------------|----------------------|----------------------|----------------------|-----|-------|----------|
| GaInP | 0.5 | 5000 | 174.541 | 9×10^{-22} | 6×10^{-6} | 3.3 | 3 | -10 |
| GaAs | 0.5 | 5000 | 175.734 | 7×10^{-16} | 1×10^{-4} | 2.8 | 3 | -10 |
| Ge | 0.5 | 45 | 278.915 | 4.3×10^{-8} | 3.5 | 2 | 3 | -1.8 |

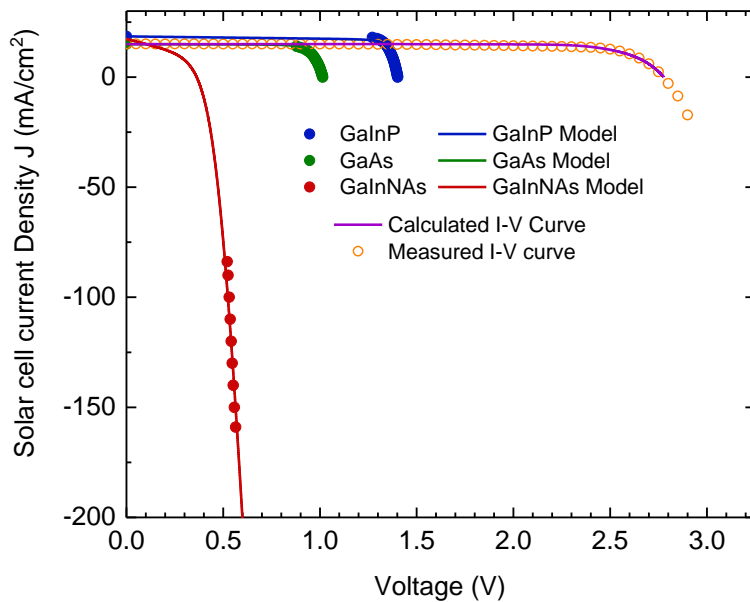
Table 3.5: Parameters for SPECTROLAB cell

| Junction | R_s [Ω] | R_{sh} [Ω] | J_{ph} [A/m^2] | J_{01} [A/m^2] | J_{02} [A/m^2] | n | n_m | V_{bd} |
|----------|--------------------|-----------------------|----------------------|----------------------|----------------------|------|-------|----------|
| GaInP | 0.5 | 5000 | 171.029 | 9×10^{-22} | 1.8×10^{-5} | 3.25 | 3 | -10 |
| GaAs | 0.5 | 5000 | 172.659 | 1×10^{-15} | 2.2×10^{-4} | 2.8 | 3 | -10 |
| Ge | 0.5 | 45 | 303.002 | 1×10^{-7} | 25 | 1.5 | 3 | -1.8 |

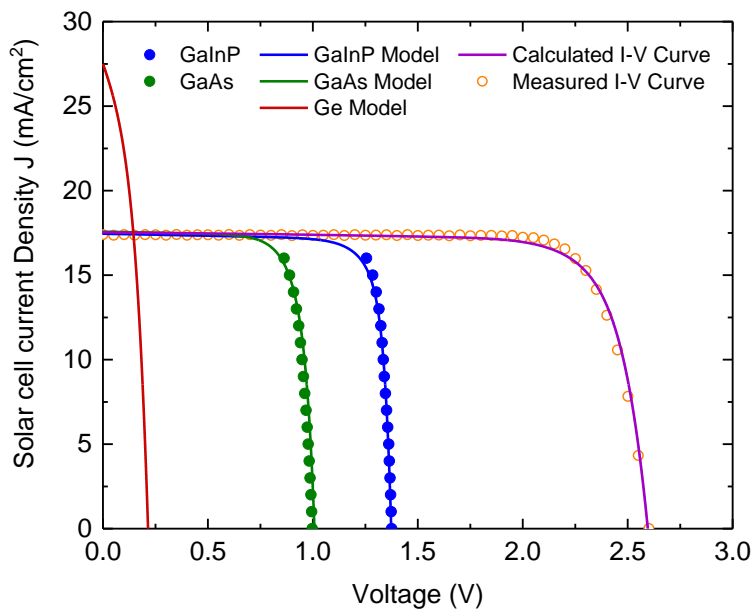
In the process of finding these parameters, we were able to understand how they individually affected the I-V curve. For example, changing the R_s affected the smoothness of the knee of the curve whereas the changing of the R_{sh} affected the bending of the curve. For the bottom junction of the Solar Junction cell, we had to fit our calculated I-V curve which was in the high negative current density region in order to obtain a model in the positive current density region. Using the parameters from tables 3.3, 3.4 and 3.5 above, we created interpolation functions for $J(V)$ vs V so that we can find the maximum power point. It is at this maximum power point that we calculate the optical losses of the solar cell.



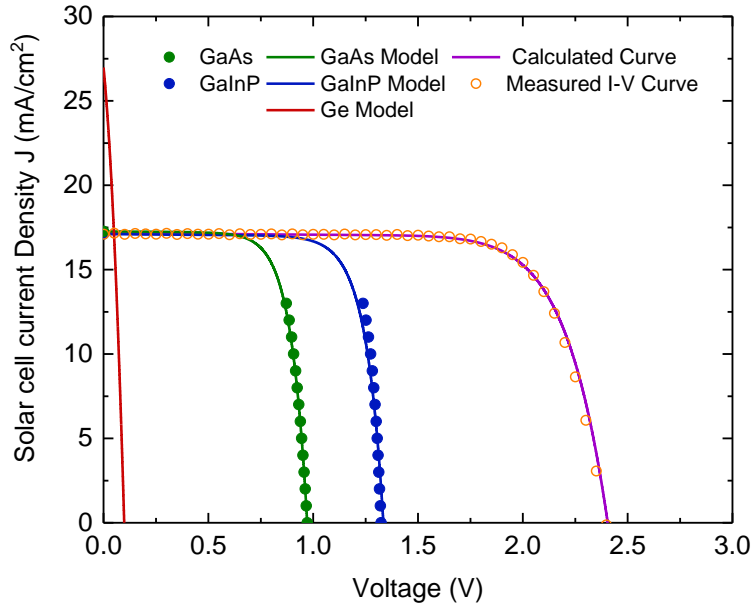
(a) Solar Junction positive J region



(b) Solar Junction negative J region



(c) EMCORE



(d) SPECTROLAB

Figure 28: I-V Curves using double diode model

3.5 Losses from three different solar cells

One of the main accomplishments of this study is that we were able to extract the loss parameters for each subcell based on the calculated I-V curves. The formulas used for calculating each of the loss parameters are shown in the table 3.6 below [47]. Note that in the formulas for thermalization and transmission loss, S_{AM0} is the AM0 spectral irradiance in units $\frac{W}{m^2 \cdot eV}$ and the integration is performed over the range of the EQE.

Table 3.6: Energy Loss formulas in power density

| | |
|----------------------------|--|
| EM (Radiative Emission) | $E_{g_i} R_{ext_{i \rightarrow 0}}$ |
| LC (Luminescence coupling) | $E_{g_i} R_{ext_{i \rightarrow i+1}} = E_{g_i} R_{ext_{i \rightarrow 0}}$ |
| NR (Nonradiative emission) | $E_{g_i} \left(R_{sun_i} + R_{ext_{i-1 \rightarrow i}} - R_{ext_{i \rightarrow i+1}} - R_{ext_{i \rightarrow 0}} - \frac{J}{q} \right)$ |
| TH (Thermalization loss) | $\int EQE_i(E) S_{AM0}(E) dE - R_{sun_i} E_{g_i}$ $+ R_{ext_{i-1 \rightarrow i}} (E_{g_{i-1}} - E_{g_i})$ |
| TR (Transmission loss) | $\int S_{AM0}(E) dE - \sum \int EQE_i(E) S_{AM0}(E) dE$ |
| JN (Junction loss) | $J \left(\frac{E_{g_i}}{q} - V_{max_i} \right)$ |

The losses will be presented as a ratio of the total AM0 1Sun input calculated as $\int S_{AM0}(E) dE$ where S_{AM0} is the AM0 spectral irradiance in units $\frac{W}{m^2 \cdot eV}$ and the integration is performed over the range of the spectral irradiance. Tables 3.7, 3.8, 3.9 present the losses for the three different solar cells. The “AM0 1sun” column shows the input ratios for the top, middle and bottom junctions which are calculated as $\frac{\int EQE_i(E) S_{AM0}(E) dE}{\int S_{AM0}(E) dE}$. The power output column is calculated as $\frac{J_{max} V_{max}}{\int S_{AM0}(E) dE}$ and it represents a ratio of incident power to max power extracted in the load. The power output from the experimentally measured IV curve is also presented in order to compare with the value from our calculated IV curve.

The EM and NR are losses due to radiative and nonradiative recombination respectively and the LC is radiative recombination from junction i that couples into

junction $i + 1$. The TH is a loss that describes how many of excited carriers are lost to thermalization. The JN is an energy loss that arises from the fact that the maximum energy we can use is at the maximum power point and the rest of the energy is lost to the junction when carriers transport across the junction to the respective contacts.

Table 3.7: Loss parameters for Solar Junction cell

| Solar Junction | | | | | | | |
|---|----------|-----------|--------------------------|--------------|-----------|-----------|--------------|
| | AM0 1sun | TH | EM | LC | NR | JN | Power Output |
| Top | 0.328735 | 0.0701294 | 0.0000166224 | 0.000203625 | 0.0637247 | 0.0544585 | 0.138591 |
| Middle | 0.182453 | 0.0250321 | 6.46363×10^{-6} | 0.0000814579 | 0.0113468 | 0.0537977 | 0.0922766 |
| Bottom | 0.154294 | 0.0329577 | 9.99423×10^{-7} | - | 0.0249549 | 0.0813247 | 0.015106 |
| TR | 0.334518 | - | - | - | - | - | - |
| Total | 0.998527 | 0.128119 | 0.0000240855 | 0.000285083 | 0.100026 | 0.189581 | 0.245974 |
| Conversion Efficiency/Power Output from Measured IV curve | | | | | | | 0.240474 |

In the top junction, 32.9 % of the solar energy is absorbed and 13.9 % is converted to electric energy, while the remainder goes into 7.0 % TH loss, 5.4% JN loss and 6.4 % NR loss. In the middle junction, 18.2% of the solar energy is absorbed and 9.2% is converted to electric energy, while the rest goes into 2.5% TH loss, 5.4 % JN loss and 1.1 % NR loss. For the bottom junction, 15.4 % of the incident solar energy is absorbed and 1.5% is converted to electric energy, while the rest goes into 3.3 % TH loss, 8.1 % JN loss and 2.4% NR loss. Of the total incident solar energy on this cell, 24.6 % is converted to electric energy while 12.8% goes into TH loss, 19.0 % goes into JN loss, and 10.0 % goes into NR loss. Our measured I-V curve shows that 24.0 % of the incident solar energy is converted to electric energy. Therefore, when all the losses are accounted and added to predicted power output, the sum totals ~ 1 . The predicted maximum power from the sum of each individual subset is very close to the

max power measured from the actual I-V curve measurement of the multijunction solar cell under AM 0 illumination.

Table 3.8: Loss parameters for EMCORE cell

| EMCORE | | | | | | | |
|---|----------|-----------|--------------------------|------------------------|-----------|-----------|--------------|
| | AM0 1sun | TH | EM | LC | NR | JN | Power Output |
| Top | 0.315051 | 0.0716145 | 5.02367×10^{-7} | 6.154×10^{-6} | 0.0185788 | 0.0772531 | 0.145241 |
| Middle | 0.217416 | 0.0349979 | 5.23577×10^{-6} | 0.0000659837 | 0.0152016 | 0.0666445 | 0.100572 |
| Bottom | 0.219289 | 0.0765686 | 2.44345×10^{-6} | - | 0.060321 | 0.0640739 | 0.0183549 |
| TR | 0.248244 | - | - | - | - | - | - |
| Total | 0.997746 | 0.183181 | 8.18158×10^{-6} | 0.0000721377 | 0.0941014 | 0.207971 | 0.264168 |
| Conversion Efficiency/Power Output from Measured IV curve | | | | | | | 0.270171 |

In the top junction, 31.5 % of the solar energy is absorbed and 14.5 % is converted to electric energy, while the remainder goes into 7.2 % TH loss, 7.7 % JN loss and 1.9 % NR loss. In the middle junction, 21.7 % of the solar energy is absorbed and 10.0 % is converted to electric energy, while the rest goes into 3.5% TH loss, 6.6% JN loss and 1.5% NR loss. For the bottom junction, 21.9 % of the incident solar energy is absorbed and 1.8% is converted to electric energy, while the rest goes into 7.6 % TH loss, 6.4 % JN loss and 6.0 % NR loss. Of the total incident solar energy on this cell, 26.4 % is converted to electric energy while 18.3% goes into TH loss, 20.7% goes into JN loss, and 9.4% goes into NR loss. Our measured IV curve reports 27.0 % of the incident solar energy as converted to electric energy. This is in agreement with the sum of power outputs of individual junctions considering an uncertainty of at least 2 % in our measurements.

Table 3.9: Loss parameters for SPECTROLAB cell

| SPECTROLAB | | | | | | | |
|---|----------|-----------|--------------------------|--------------------------|-----------|-----------|--------------|
| | AM0 1sun | TH | EM | LC | NR | JN | Power Output |
| Top | 0.304456 | 0.0747707 | 1.61111×10^{-7} | 1.97361×10^{-6} | 0.0174135 | 0.0808361 | 0.129823 |
| Middle | 0.213561 | 0.03428 | 8.36361×10^{-7} | 0.0000105402 | 0.015251 | 0.0724466 | 0.0915837 |
| Bottom | 0.237875 | 0.0828305 | 3.00762×10^{-6} | - | 0.0742164 | 0.0744317 | 0.00640145 |
| TR | 0.244107 | - | - | - | - | - | - |
| Total | 0.998409 | 0.191881 | 4.00509×10^{-6} | 0.0000125139 | 0.106881 | 0.227714 | 0.227808 |
| Conversion Efficiency/Power Output from Measured IV curve | | | | | | | 0.230001 |

In the top junction, 30.4 % of the solar energy is absorbed and 12.9 % is converted to electric energy, while the remainder goes into 7.4 % TH loss, 8.0 % JN loss and 1.7 % NR loss. In the middle junction, 21.3 % of the solar energy is absorbed and 9.2% is converted to electric energy, while the rest goes into 3.4% TH loss, 7.2% JN loss and 1.5% NR loss. For the bottom junction, 23.7 % of the incident solar energy is absorbed and 0.6% is converted to electric energy, while the rest goes into 8.2 % TH loss, 7.4 % JN loss and 7.4 % NR loss. Of the total incident solar energy on this cell, 22.7 % is converted to electric energy while 19.1 % goes into TH loss, 22.7 % goes into JN loss, and 10.6 % goes into NR loss. Our measured IV curve predicts that 23.0% of the incident solar energy is converted to electric energy. There is a 1.32% deviation between the two values for conversion efficiency.

In order to better compare the losses for all three cells, it is important to know the J_{\max} and V_{\max} values for each junction for each cell shown in table 3.10 below.

Table 3.10: J_{max} and V_{max} values for each junction for each cell

| Cell | J_{max} (mA/cm ²) | V_{max1} (V) | V_{max2} (V) | V_{max3} (V) |
|----------------|---------------------------------|----------------|----------------|----------------|
| Solar Junction | 13.9165 | 1.3429 | 0.8941 | 0.1463 |
| EMCORE | 16.1089 | 1.2157 | 0.8418 | 0.1536 |
| SPECTROLAB | 15.7971 | 1.1081 | 0.7817 | 0.0546 |

The two most important loss parameters we were able to extract through all the EL measurements and the subsequent calculations are the NR and JN losses. For NR losses, knowledge of the $R_{ext_{i \rightarrow 0}}$ for each junction was necessary and to get the JN losses for each junction, we needed the V_{max_i} for that junction which was extracted from each subcell's I-V curve. We see that the SPECTROLAB cell has the highest total NR and JN losses. The EMCORE and SPECTROLAB cells consist of the GaInP/GaAs/Ge junctions whereas the Solar Junction cell is made of GaInP/GaAs/GaInNAs junctions. To understand why the SPECTROLAB has a higher NR loss, it is appropriate to only compare with the EMCORE cell which has the same junctions. If we recall from the formula for NR loss, we see that for each junction, it is calculated by subtracting the power contribution of the maximum solar cell current density and energy losses (EM loss, LC loss) from the incident solar power on the junction (R_{sun} value and LC from previous junction if applicable). As mentioned earlier in this chapter, the R_{sun} values are different for each junction and could contribute to the high NR loss. More specifically, the R_{sun} value for the bottom junction is the highest for this cell and the EM and LC loss are comparably lower. In addition, compared to the J_{max} value for EMCORE, the J_{max} value for SPECTROLAB

is lower. Therefore, with a higher R_{sun} value and lower values for all other parameters in the calculation, we arrive at a higher NR loss for the bottom junction. The higher value for the bottom junction contributes to a higher overall NR loss for the SPECTROLAB cell.

The JN loss for the SPECTROLAB cell is also the highest because the V_{max} values for each junction are lower than those for the EMCORE cell. From the formula for JN loss, we have to subtract the V_{max} value from the bandgap of that junction. For example, for the top junction, the bandgaps stay roughly the same so the lower the V_{max} value, the higher our JN loss. This makes sense because more energy is lost to the junction if the maximum energy we can use is lower. The combination of overall lower J_{max} and V_{max} values contributes to a lower power output for the SPECTROLAB cell.

It is appropriate to compare the results from the EMCORE and SPECTROLAB cell to the solar cell used in the Chen et. al. paper as it consists of the same three junctions. For the EMCORE and SPECTROLAB cell, the total TH, NR and JN losses are larger than those presented in the paper and total power output is lower than that presented in the paper. It is important to note that since we were not able to take data on the bottom junction, we used the double diode model to model that junction's IV curve and used the band gap energies presented in the paper. Therefore, it is possible that the deviation of the loss values from those presented in the paper is due to this fact.

Note that in general, the percentages of radiative recombination or EM loss and LC loss are very small for all three cells. However, the relatively high values of EM and

LC loss for the Solar Junction cell show that less of the incident solar energy is going to nonradiative recombination. A higher EM value corresponds to a higher external luminescence quantum efficiency y_{ext} and a higher V_{oc} . A higher V_{oc} suggests a possible higher V_{max} and ultimately a higher power output.

There are several reasons why the EMCORE cell might have a higher efficiency as compared to the SPECTROLAB cell. For example, the EMCORE cell might have been better optimized in terms of the thicknesses of each of the layers and doping. Thickness optimization might, for example, result in less series resistance or the depletion region being smaller. Regarding doping, if the diffusion length of the minority carriers is too long, the carriers will have a lower probability of reaching the junction and will recombine. The EMCORE cell also has a smaller area and this could play a role in decreasing the series resistance losses. In general, the larger the bandgap E_g , the larger the V_{oc} . For the EMCORE cell, we can see that the bandgap is much higher for the GaInP junction than for the SPECTROLAB cell and therefore we see a higher V_{max} . Using Ge as the bottom junction in a triple-junction cell is common as it absorbs more radiation leading to lower transmission loss TR. The bottom junction of the Solar Junction cell is GaInNAs which has a higher bandgap and as a result, a higher V_{oc} but there is also more TR loss. Thus, there is a trade-off between the V_{oc} and the TR loss which must be considered.

There are several factors which must be considered when explaining the behavior of a solar cell. The loss tables presented in this chapter provide for an easy way to understand where the incident solar radiation is being lost.

Chapter 4: Conclusions

In this work, we examined three different multijunction solar cells and it was shown that each subcell within the multijunction stack can be characterized in detail by taking absolute electroluminescence data.

In chapter 1, we looked at the physics of solar cells and explained that the measurement of the electroluminescence (EL) response of solar cells is an important technique to characterize solar cells. We also derived the I-V characteristic and highlighted some of the fundamental losses in solar cells. In chapter 2, we discussed the hyperspectral imaging system which was used to take our EL data and discussed some of the post-processing necessary in order to use the data in our calculations. Furthermore, in order to understand the data taken, we had to apply a calibration factor for which we took spectral irradiance data on a QTH-illuminated pinhole aperture. Once we obtained calibrated EL data from measurements of a few multijunction solar cells, we were ready to follow a series of calculations, detailed in chapter 3, to obtain the I-V curves and ultimately the loss parameters for each of our solar cells and the subcells within them.

Obtaining the I-V curves and loss parameters helps us understand how efficiently the solar cell uses the incident solar energy. Understanding that various loss mechanisms that reduce the overall power conversion efficiency of the solar cells is extremely important. This information plays a key role in the solar cell industry as it helps determine how to best maximize the output power. Gleaning this wealth of information from simple EL measurements proves the convenience of the methodology and can be used in future experiments.

We analyzed three solar cells in this paper: “Solar Junction” with GaInP/GaAs/GaInNAs junctions, “EMCORE” with GaInP/GaAs/Ge junctions and “SPECTROLAB” with GaInP/GaAs/Ge junctions. After performing our analysis we noticed that the EMCORE cell had the highest efficiency. One possible reason for this is that this cell might have been optimized for thicknesses of each of the layers and doping. Through the loss tables presented for each of the cells, we are able to see how the incident solar radiation is being used. By considering other factors that affect the solar cell performance, improvements can be made in photonic engineering to improve the cell’s efficiency. As an example, we saw that the transmission loss for the Solar Junction cell was higher than the other two cells and one possible reason for this is that the bottom junction’s bandgap is higher than those of the other two cells. A larger bandgap leads to a larger V_{oc} , but a higher transmission loss since part of the incident radiation is not absorbed by the bottom junction. Likewise, several material properties must be optimized when designing a solar cell to improve the cell’s efficiency.

Using the methodology outlined in this paper, one can perform the same analysis for solar cells made from different semiconductor materials. Further experiments also include using photoluminescence (PL) to characterize solar cells which will yield results which will allow us to determine the saturation current or provide us with a mapping of the quasi-Fermi level splitting.

Bibliography

- [1] “Solar Photovoltaic Cell Basics,” *Energy.gov*. [Online]. Available:
<https://www.energy.gov/eere/solar/articles/solar-photovoltaic-cell-basics>.
[Accessed: 17-Mar-2020].
- [2] “Single Crystalline Silicon | PVEducation.” [Online]. Available:
<https://www.pveducation.org/pvcdrom/manufacturing-si-cells/single-crystalline-silicon>. [Accessed: 17-Mar-2020].
- [3] “Multi Crystalline Silicon | PVEducation.” [Online]. Available:
<https://www.pveducation.org/pvcdrom/manufacturing-si-cells/multi-crystalline-silicon>. [Accessed: 17-Mar-2020].
- [4] “Best Research-Cell Efficiency Chart.” [Online]. Available:
<https://www.nrel.gov/pv/cell-efficiency.html>. [Accessed: 17-Mar-2020].
- [5] “Solar Photovoltaic Technology Basics.” [Online]. Available:
<https://www.nrel.gov/research/re-photovoltaics.html>. [Accessed: 17-Mar-2020].
- [6] J. Nelson, *The physics of solar cells*. London : River Edge, NJ: Imperial College Press ; Distributed by World Scientific Pub. Co, 2003.
- [7] Luque and S. Hegedus, Eds., *Handbook of photovoltaic science and engineering*, 2nd ed. Chichester, West Sussex, U.K: Wiley, 2011.
- [8] S. M. Sze, *Physics of semiconductor devices*, 2nd ed. New York: Wiley, 1981.
- [9] P. Würfel and U. Würfel, *Physics of solar cells: from basic principles to advanced concepts*, 3rd edition. Weinheim: Wiley-VCH Verlag GmbH & Co. KGaA, 2016.

- [10] “V. Air Mass,” *Engineering LibreTexts*, 03-Nov-2018.
[https://eng.libretexts.org/Bookshelves/Materials_Science/Supplemental_Modules_\(Materials_Science\)/The_Science_of_Solar/Solar_Basics/B._Basics_of_the_Sun/V._Air_Mass](https://eng.libretexts.org/Bookshelves/Materials_Science/Supplemental_Modules_(Materials_Science)/The_Science_of_Solar/Solar_Basics/B._Basics_of_the_Sun/V._Air_Mass) (accessed Mar. 24, 2020).
- [11] B. G. Streetman and S. Banerjee, *Solid state electronic devices*, 6th ed. Upper Saddle River, N.J: Pearson/Prentice Hall, 2006.
- [12] D. A. Neamen, *Semiconductor physics and devices: basic principles*, 4th ed. New York, NY: McGraw-Hill, 2012.
- [13] S. J. Fonash, *Solar cell device physics*, 2nd ed. Burlington, MA: Academic Press/Elsevier, 2010.
- [14] A. J. McEvoy, L. Castañer, and T. Markvart, *Solar cells: materials, manufacture and operation*, 2nd ed. Oxford: Elsevier, 2013.
- [15] W. Shockley and W. T. Read, “Statistics of the Recombinations of Holes and Electrons,” *Phys. Rev.*, vol. 87, no. 5, pp. 835–842, Sep. 1952, doi: 10.1103/PhysRev.87.835.
- [16] W. Shockley and H. J. Queisser, “Detailed Balance Limit of Efficiency of p-n Junction Solar Cells,” *Journal of Applied Physics*, vol. 32, no. 3, pp. 510–519, Mar. 1961, doi: 10.1063/1.1736034.
- [17] T. Kirchartz and U. Rau, “Detailed balance and reciprocity in solar cells,” *phys. stat. sol. (a)*, vol. 205, no. 12, pp. 2737–2751, Dec. 2008, doi: 10.1002/pssa.200880458.

- [18] G. L. Araújo and A. Martí, “Absolute limiting efficiencies for photovoltaic energy conversion,” *Solar Energy Materials and Solar Cells*, vol. 33, no. 2, pp. 213–240, Jun. 1994, doi: 10.1016/0927-0248(94)90209-7.
- [19] X. Wang and M. S. Lundstrom, “On the Use of Rau’s Reciprocity to Deduce External Radiative Efficiency in Solar Cells,” *IEEE J. Photovoltaics*, vol. 3, no. 4, pp. 1348–1353, Oct. 2013, doi: 10.1109/JPHOTOV.2013.2278658.
- [20] U. Rau, D. Abou-Ras, and T. Kirchartz, Eds., *Advanced characterization techniques for thin film solar cells*. Weinheim, Germany: Wiley-VCH, 2011.
- [21] U. Rau, “Reciprocity relation between photovoltaic quantum efficiency and electroluminescent emission of solar cells,” *Phys. Rev. B*, vol. 76, no. 8, p. 085303, Aug. 2007, doi: 10.1103/PhysRevB.76.085303.
- [22] T. Kirchartz, A. Helbig, W. Reetz, M. Reuter, J. H. Werner, and U. Rau, “Reciprocity between electroluminescence and quantum efficiency used for the characterization of silicon solar cells,” *Prog. Photovolt: Res. Appl.*, vol. 17, no. 6, pp. 394–402, Sep. 2009, doi: 10.1002/pip.895.
- [23] T. Kirchartz, U. Rau, M. Kurth, J. Mattheis, and J. H. Werner, “Comparative study of electroluminescence from Cu(In,Ga)Se₂ and Si solar cells,” *Thin Solid Films*, vol. 515, no. 15, pp. 6238–6242, May 2007, doi: 10.1016/j.tsf.2006.12.105.
- [24] T. Kirchartz and U. Rau, “Electroluminescence analysis of high efficiency Cu(In,Ga)Se₂ solar cells,” *Journal of Applied Physics*, vol. 102, no. 10, p. 104510, Nov. 2007, doi: 10.1063/1.2817959.

- [25] T. Kirchartz, U. Rau, M. Hermle, A. W. Bett, A. Helbig, and J. H. Werner, “Internal voltages in GaInP/GaInAs/Ge multijunction solar cells determined by electroluminescence measurements,” *Appl. Phys. Lett.*, vol. 92, no. 12, p. 123502, Mar. 2008, doi: 10.1063/1.2903101.
- [26] R. Hoheisel, D. Scheiman, S. Messenger, P. Jenkins, and R. Walters, “Detailed Characterization of the Radiation Response of Multijunction Solar Cells Using Electroluminescence Measurements,” *IEEE Trans. Nucl. Sci.*, vol. 62, no. 6, pp. 2894–2898, Dec. 2015, doi: 10.1109/TNS.2015.2498838.
- [27] O. D. Miller, E. Yablonovitch, and S. R. Kurtz, “Strong Internal and External Luminescence as Solar Cells Approach the Shockley–Queisser Limit,” *IEEE J. Photovoltaics*, vol. 2, no. 3, pp. 303–311, Jul. 2012, doi: 10.1109/JPHOTOV.2012.2198434.
- [28] A. Delamarre, “Characterization of solar cells using electroluminescence and photoluminescence hyperspectral images,” *J. Photon. Energy*, vol. 2, no. 1, p. 027004, Jul. 2012, doi: 10.1117/1.JPE.2.027004.
- [29] S. Roensch, R. Hoheisel, F. Dimroth, and A. W. Bett, “Subcell I-V characteristic analysis of GaInP/GaInAs/Ge solar cells using electroluminescence measurements,” *Appl. Phys. Lett.*, vol. 98, no. 25, p. 251113, Jun. 2011, doi: 10.1063/1.3601472.
- [30] L. C. Hirst and N. J. Ekins-Daukes, “Fundamental losses in solar cells,” *Prog. Photovolt: Res. Appl.*, vol. 19, no. 3, pp. 286–293, May 2011, doi: 10.1002/pip.1024.

- [31] M. A. Green, “Third generation photovoltaics: Ultra-high conversion efficiency at low cost,” *Prog. Photovolt: Res. Appl.*, vol. 9, no. 2, pp. 123–135, Mar. 2001, doi: 10.1002/pip.360.
- [32] F. H. Alharbi and S. Kais, “Theoretical limits of photovoltaics efficiency and possible improvements by intuitive approaches learned from photosynthesis and quantum coherence,” *Renewable and Sustainable Energy Reviews*, vol. 43, pp. 1073–1089, Mar. 2015, doi: 10.1016/j.rser.2014.11.101.
- [33] T. Markvart, “Thermodynamics of losses in photovoltaic conversion,” *Appl. Phys. Lett.*, vol. 91, no. 6, p. 064102, Aug. 2007, doi: 10.1063/1.2766857.
- [34] T. Oku, *Solar cells and energy materials*. Berlin Boston: De Gruyter, 2017.
- [35] D. Ding, S. R. Johnson, S.-Q. Yu, S.-N. Wu, and Y.-H. Zhang, “A semi-analytical model for semiconductor solar cells,” *Journal of Applied Physics*, vol. 110, no. 12, p. 123104, Dec. 2011, doi: 10.1063/1.3671061.
- [36] M. A. Steiner et al., “Measuring IV curves and subcell photocurrents in the presence of luminescent coupling,” in *2012 IEEE 38th Photovoltaic Specialists Conference (PVSC) PART 2*, Austin, TX, USA, 2012, pp. 1–11, doi: 10.1109/PVSC-Vol2.2012.6656785.
- [37] D. Lan, J. F. Geisz, M. A. Steiner, I. Garcia, D. J. Friedman, and M. A. Green, “Improved modeling of photoluminescent and electroluminescent coupling in multijunction solar cells,” *Solar Energy Materials and Solar Cells*, vol. 143, pp. 48–51, Dec. 2015, doi: 10.1016/j.solmat.2015.06.036.
- [38] “GRAND-EOS | Hyperspectral widefield imager | Visible and SWIR,” photonetc. <http://photonetc.com/en/grand-eos.html> (accessed Mar. 24, 2020).

- [39] S. Marcet, M. Verhaegen, S. Blais-Ouellette, and R. Martel, “Raman spectroscopy hyperspectral imager based on Bragg tunable filters,” presented at the Photonics North 2012, Montreal, Canada, 2012, p. 84121J, doi: 10.1117/12.2000479.
- [40] D. Gagnon and L.-I. Dion-Bertrand, “Widely Tunable Filter Technology and Measurement of Critical Specifications.” 09-Sep-2015.
- [41] “Volume Bragg Tunable Filter,” *photonetc*. <http://photonetc.com/en/volume-bragg-tunable-filter.html> (accessed Mar. 24, 2020).
- [42] E. Gaufrès et al., “Hyperspectral Raman imaging using Bragg tunable filters of graphene and other low-dimensional materials: Hyperspectral Raman imaging using Bragg tunable filters of graphene and other low-dimensional materials,” *J. Raman Spectrosc.*, vol. 49, no. 1, pp. 174–182, Jan. 2018, doi: 10.1002/jrs.5298.
- [43] M. Verhaegen, S. Lessard, and S. Blais-Ouellette, “Narrow band SWIR hyperspectral imaging: a new approach based on volume Bragg grating,” presented at the SPIE Defense, Security, and Sensing, Baltimore, Maryland, USA, 2012, p. 83740G, doi: 10.1117/12.920811.
- [44] D. Roxbury et al., “Hyperspectral Microscopy of Near-Infrared Fluorescence Enables 17-Chirality Carbon Nanotube Imaging,” *Sci Rep*, vol. 5, no. 1, p. 14167, Nov. 2015, doi: 10.1038/srep14167.
- [45] Photon etc. , “PHySpec User Guide.” .
- [46] J. O. Akinlami and A. O. Ashamu, “Optical properties of GaAs,” *J. Semicond.*, vol. 34, no. 3, p. 032002, Mar. 2013, doi: 10.1088/1674-4926/34/3/032002.

- [47] S. Chen et al., “Thorough subcells diagnosis in a multi-junction solar cell via absolute electroluminescence-efficiency measurements,” *Sci Rep*, vol. 5, no. 1, p. 7836, Jul. 2015, doi: 10.1038/srep07836.
- [48] J. P. Babaro, K. G. West, and B. H. Hamadani, “Spectral response measurements of multijunction solar cells with low shunt resistance and breakdown voltages,” *Energy Sci Eng*, vol. 4, no. 6, pp. 372–382, Nov. 2016, doi: 10.1002/ese3.141.
- [49] M. Yoshita et al., “Absolute electroluminescence imaging of multi-junction solar cells and calibration standards,” in *2015 IEEE 42nd Photovoltaic Specialist Conference (PVSC)*, New Orleans, LA, 2015, pp. 1–4, doi: 10.1109/PVSC.2015.7356199.
- [50] R. Carron et al., “Bandgap of thin film solar cell absorbers: A comparison of various determination methods,” *Thin Solid Films*, vol. 669, pp. 482–486, Jan. 2019, doi: 10.1016/j.tsf.2018.11.017.
- [51] F. Masmoudi, F. Ben Salem, and N. Derbel, “Single and double diode models for conventional mono-crystalline solar cell with extraction of internal parameters,” in *2016 13th International Multi-Conference on Systems, Signals & Devices (SSD)*, Leipzig, Germany, 2016, pp. 720–728, doi: 10.1109/SSD.2016.7473725.